

# Linear stability analysis and nonlinear simulations of convective dissolution in an inclined porous layer between impermeable surfaces

Cite as: Chaos **32**, 113110 (2022); <https://doi.org/10.1063/5.0089326>

Submitted: 24 February 2022 • Accepted: 28 September 2022 • Published Online: 02 November 2022

 R. M. Lucena,  J. Pontes,  A. De Wit, et al.



View Online



Export Citation



CrossMark

## ARTICLES YOU MAY BE INTERESTED IN

[New 4D and 3D models of chaotic systems developed from the dynamic behavior of nuclear reactors](#)

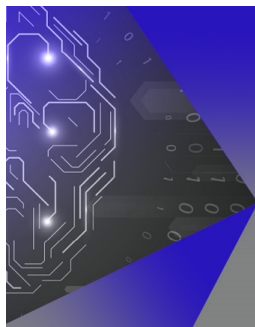
Chaos: An Interdisciplinary Journal of Nonlinear Science **32**, 113108 (2022); <https://doi.org/10.1063/5.0090518>

[Cupolets in a chaotic neuron model](#)

Chaos: An Interdisciplinary Journal of Nonlinear Science **32**, 113104 (2022); <https://doi.org/10.1063/5.0101667>

[Dual-domain analysis of gun violence incidents in the United States](#)

Chaos: An Interdisciplinary Journal of Nonlinear Science **32**, 111101 (2022); <https://doi.org/10.1063/5.0120822>



## APL Machine Learning

Machine Learning for Applied Physics  
Applied Physics for Machine Learning

Now Open for Submissions

# Linear stability analysis and nonlinear simulations of convective dissolution in an inclined porous layer between impermeable surfaces

Cite as: Chaos 32, 113110 (2022); doi: 10.1063/5.0089326

Submitted: 24 February 2022 · Accepted: 28 September 2022 ·

Published Online: 2 November 2022



View Online



Export Citation



CrossMark

R. M. Lucena,<sup>1,a)</sup>  J. Pontes,<sup>1</sup>  A. De Wit,<sup>2</sup>  G. R. Anjos,<sup>3</sup>  and N. Mangiavacchi<sup>1</sup> 

## AFFILIATIONS

<sup>1</sup>Group of Environmental Studies for Water Reservoirs—GESAR, Rio de Janeiro State University, 20940-903 Rio de Janeiro, RJ, Brazil

<sup>2</sup>Nonlinear Physical Chemistry Unit, CP 231, Faculté des Sciences, Université Libre de Bruxelles (ULB), 1050 Brussels, Belgium

<sup>3</sup>COPPE—Department of Mechanical Engineering, Universidade Federal do Rio de Janeiro, 21941-914 Rio de Janeiro, Brazil

<sup>a)</sup>Author to whom correspondence should be addressed: [rachel.lucena@gmail.com](mailto:rachel.lucena@gmail.com)

## ABSTRACT

Convective dissolution can occur in porous media when a given solute dissolves in a host layer from above and increases the density of the host solution. Buoyancy-driven fingering can then develop, which increases the transfer flux of the solute. We investigate here numerically the properties of this convective dissolution when the porous host layer is inclined by an angle  $\theta$  relative to the horizontal direction. We consider an incompressible flow in porous media governed by Darcy's law, driven by density gradients associated with the concentration of the dissolving solute. The model problem focuses on the case of a very long (infinite) tilted porous layer limited by two parallel impermeable surfaces. A linear stability analysis and nonlinear simulations are performed using the Boussinesq approximation. A vorticity-stream function formulation is adopted to solve the two-dimensional hydrodynamic field through the finite element method. We find that the inclination of the interface decreases the growth rate of the instability and the range of unstable wavenumbers, delaying or even suppressing the onset of the fingering instability. Moreover, it introduces a drift velocity on the perturbations, which is characterized here in both the linear stability analysis and the nonlinear simulations.

Published under an exclusive license by AIP Publishing. <https://doi.org/10.1063/5.0089326>

In Carbon Capture and Sequestration (CCS) techniques, convective dissolution of CO<sub>2</sub> in host saline aquifers favors its long-term storage in those deep geological porous layers. We examine here the mechanisms at play when the host porous layer is inclined at an arbitrary angle with respect to the horizontal direction. We study numerically the stability and nonlinear evolution of convective dissolution in the case where a very long (infinite) inclined layer of porous media is limited by two parallel impermeable surfaces. The linearized governing equations for the disturbances are solved numerically by a Chebyshev spectral collocation method. The nonlinear equations are solved by employing the finite element method, providing further insight into the dynamics of the nonlinear fingering instability in the vicinity of an inclined interface. We found that increasing the slope of the interface decreases the instability growth rate and the range of unstable wave numbers, delaying or even suppressing the onset of the fingering instability.

## I. INTRODUCTION

In the context of global warming, there is currently increased interest to characterize the physico-chemical mechanisms at play during carbon capture and sequestration. In this technique, carbon dioxide is captured at the exhaust of power plants, steel, cement, fertilizer, and other manufacturing units, potentially for hydrogen production and also in combination with biofuels for energy (a potential net negative emissions process). After being captured, CO<sub>2</sub> is liquefied and transferred to sequestration sites where it is injected into deep geologic strata.<sup>1</sup> There, a two-layer stratification of supercritical CO<sub>2</sub> above the host phase is formed. When CO<sub>2</sub> dissolves in the lower partially miscible host layer, it increases its density. This induces a buoyancy-driven instability creating CO<sub>2</sub>-rich fingers sinking down convectively toward the bottom of the host phase.<sup>2</sup> To quantify the amount of CO<sub>2</sub> that can be stored for given specific geological conditions, numerous works have analyzed both experimentally and theoretically the properties of this convective

dissolution instability,<sup>3–22</sup> considering a horizontal interface between the upper CO<sub>2</sub> layer and the lower host phase. In practice, however, this interface is not necessarily horizontal as local topologies of the impermeable caprock imprisoning the CO<sub>2</sub> pool can be inclined with regard to the horizontal ones.

Similarly, a solid phase dissolving in a liquid layer can also trigger convective dissolution, the properties of which will depend on the angle of inclination of the solid block with regard to the vertical.<sup>23</sup>

Laboratory experiments and a theoretical model were developed by MacMinn and Juanes<sup>12</sup> to study the effectiveness of convective dissolution in inclined aquifers. They have demonstrated that convective dissolution can arrest the upslope migration of a buoyant current. They found that a small amount of slope is beneficial to dissolution relative to a horizontal aquifer, leading to a sharp decrease in the lifetime of a buoyant current with only a small increase in the maximum migration distance, showing a good agreement with Hesse *et al.*<sup>10</sup> The results obtained by Hesse *et al.*<sup>10</sup> suggest that residual trapping is quite effective in sloping aquifers with small mobility ratios and high residual CO<sub>2</sub> saturation. Nevertheless, the long migration distances of CO<sub>2</sub> due to the formation of a gravity tongue may limit the volume of CO<sub>2</sub> that can be stored in sloping regional aquifers. Larger slopes lead to much larger migration distances with only a small decrease in the lifetime of the current, but residual trapping provides a strong complement to convective dissolution as the amount of slope increases.

Huppert and Woods<sup>24</sup> have analyzed the situation in which the gravity-driven flows in porous media propagate along a sloping channel, in a layer of uniform permeability. A finite volume of fluid propagates steadily along the slope under gravity and spreads diffusively owing to the gravitational acceleration normal to the boundary, as on a horizontal boundary. They concluded that, if the porosity increases or decreases with distance from the boundary, then, in the long-time asymptotic limit, a discrete release of fluid will tend to generate a discontinuity at the nose or tail of the flow respectively. Similarly, Vella and Huppert<sup>25</sup> have considered the propagation of a gravity current in a porous medium below an impermeable sloping boundary. Through laboratory and numerical experiments, they observed that, shortly after its initiation, a constant-flux gravity current begins to spread axisymmetrically. Nevertheless, at larger times, the axisymmetry is lost and the gravity current propagates predominantly downslope.

Meng and Jiang have performed numerical analyses of the solubility trapping of CO<sub>2</sub> in geological formations using 2D and 3D approaches.<sup>15</sup> These authors have conducted a dimensional study of the dissolution of CO<sub>2</sub> into the brine, which leads to a fingering instability, in a finite inclined aquifer (finite due to the boundary conditions). They concluded that the number of fingers is reduced and the interaction between them is weakened when the angle of inclination is increased.

Guerrero *et al.*<sup>26</sup> provide numerical results of the effect of inclination on CO<sub>2</sub> dissolution and thermo-solutal convection in a porous enclosure heated from below. The effect of the inclination is found to be minor when compared to the Rayleigh number and buoyancy ratio effects. Increasing the angle slightly decreases the mixing length as a consequence of the formation of preferential flow paths associated with the inclination. These preferential flow paths make mixing less efficient and give rise to zonation of

solute concentration. This effect may, in part, be associated to the finite size of the enclosure and the imposition of the impermeable lateral walls boundary conditions. Different results are found by Tsai *et al.*,<sup>27</sup> where the density-driven convection is enhanced by an inclined boundary. In this experimental study, the top interface is maintained essentially horizontal by the gravity force, while the lateral and the bottom boundaries of the cell are inclined, and the fingers are observed to move toward the lateral walls. This effect, and the observed beneficial effect on the dissolution, can be attributed to a large-scale gravity current, set up by the lateral plume movements, which is a double recirculating flow that emerges as a consequence of the interaction of the fingers with the inclined walls.

Very relevant to the subject of the present investigation, works were performed regarding inclined porous media by Wen and Chini<sup>28,29</sup> for large and moderate Rayleigh numbers, addressing both numerical simulations and linear stability analysis (LSA) of the inclined problem, for a similar geometry, but considering a steady state concentration base flow, with prescribed concentration (or temperature) conditions at the top and bottom interfaces. Similarly to the problem addressed in this work, they find a limiting angle of inclination, beyond which no fingering instability is observed.

A comprehensive review of recent results on convection in porous media is provided by Hewitt.<sup>30</sup> In this review, the basic mathematical framework for convection in porous media governed by Darcy's law is outlined, and its validity and limitations discussed. The review considers "two-sided" and "one-sided" systems, the former mimicking the classical Rayleigh–Bénard setup of a cell heated from below and cooled from above, the latter involving convection from one boundary only, which evolves in time through a series of regimes. Both setups are reviewed, and studies that incorporate additional physical effects are discussed.

To our knowledge, no linear stability analysis (LSA) of the inclined interface problem has been performed up to now for transient "one-sided" systems. Most numerical simulations on inclined domains performed in the literature only addressed finite domains with impermeable lateral walls, where the accumulation of solute at the lower side of the interface leads to the formation of strong gravity currents or inclined "two-sided" systems. The case of inclined "one-sided" systems, with no effect of lateral walls, for the transient start-up problem with impermeable, zero flux, bottom boundary condition, has not been addressed.

In this context, we study here numerically the stability and nonlinear evolution of convective dissolution in the case where the interface between the dissolving layer and the host phase is inclined with an arbitrary angle with regard to the horizontal. Specifically, we study the temporal evolution of small perturbations near an inclined interface in a saturated porous medium with buoyancy effects due to gradients of concentration of a soluble compound. In particular, we analyze the model problem where a very long (infinite) tilted layer of a porous medium is limited by two parallel impermeable surfaces. Both the upper and the lower surfaces are impermeable and non-deformable, which is an interesting theoretical simplification. It must be remarked that neither simplification corresponds to a CO<sub>2</sub>–water interface, which might in addition have a capillary fringe. Therefore, we are solving for a simplified approximation of the full problem.

The current problem can be used to explain the behavior of instability in regions where the interface is deformed since, as a first approximation, when the wavelength of the deformation is very long compared to the wavelength of the perturbation, the fact that the interface is deformed can be taken into account by its inclination with respect to the horizontal direction.

The present study is also relevant to the problem of CO<sub>2</sub> in the presence of background flow, as studied by Emami-Meybodi *et al.*,<sup>31</sup> where they find that a background flow may delay the onset of free convection when considering a dispersion effect. We can observe that, in the case of the presence of a steady and uniform background flow, the interface at the top of an unconfined (free) aquifer over a sloping boundary, will also be inclined and can be analyzed, neglecting the background flow dispersion effect already studied by Emami-Meybodi *et al.*,<sup>31</sup> employing the results obtained in this work.

The linearized governing equations for the disturbances yield a fourth-order eigenvalue problem, which is solved numerically by a spectral collocation technique with expansions in Chebyshev polynomials. It is found that the inclination of the interface has a stabilizing effect on the fluid flow while producing a lateral drift velocity on the perturbations. The nonlinear equations are then solved employing a finite element method, providing further insight into the dynamics of the nonlinear fingering instability in the vicinity of an inclined interface.

This article is organized as follows: the governing equations of the problem are first presented along with the base state solution. A linear stability analysis (LSA) is performed and the effect of inclination is studied on both semi-infinite and finite depth domains. Finally, numerical simulations of fingering generation in a thick porous layer are presented followed by the final remarks in the conclusion section.

## II. POSING THE PROBLEM AND GOVERNING EQUATIONS

In a way similar to the analysis of the horizontal case,<sup>11,32</sup> we consider buoyancy-driven fingering generated in porous media by the dissolution of a partially miscible solute in a host phase layer below it. The interface separating the dissolving layer and the host phase is inclined by an angle  $\theta$  relative to the horizontal direction. Our focus is on the lower layer where the convective dissolution dynamics takes place. As the geometry of the interface is considered not to be altered by the dissolution process and the resulting flow, the analysis applies to the general case of dissolution of a fluid<sup>33</sup> as well as of a solid layer<sup>23</sup> when neglecting porosity changes. This model is relevant in geothermal settings as well as possible industrial applications.

We use the Boussinesq approximation to account for buoyancy effects introduced by the concentration dependent density. The viscosity is assumed to be constant. The solution of the two-dimensional velocity field is not formulated in terms of the primitive variables. Instead, we adopt the vorticity-stream function formulation to accurately solve the hydrodynamic field.<sup>33,34</sup> The main advantage of such a formulation is that pressure is eliminated, therefore no special numerical treatment is required to circumvent the stability restrictions imposed by the coupling between velocity and

pressure. In this work, we will denote all dimensional variables with an asterisk (\*), while the corresponding non-dimensional variables will be denoted without an asterisk.

We consider a 2D incompressible flow in a layer of porous medium described by Darcy's law, and driven by density differences associated to the (dimensional) concentration of a solute  $c^*$ , dissolving at the upper interface as can be seen in Fig. 1. The layer is inclined with an angle  $\theta$  with respect to the horizontal line, and the coordinated system is conveniently rotated such that the  $x$  and  $y$  directions coincide with the tangent and normal directions of the impermeable interfaces. The considered numerical domain is a rectangle with width  $L_x^*$  and height  $L_y^*$ . The driving mechanism of the flow is the body force (per unit volume) associated to gravity  $\mathbf{g}^*$  and to the density of the fluid as  $\mathbf{b}^* = \mathbf{g}^* \rho^*$ , where  $\mathbf{g}^* = (g^* \sin \theta, g^* \cos \theta)$  is the gravity vector [see Fig. 1(b)]. Considering the Boussinesq approximation, the dimensional flow velocity  $\mathbf{u}^* = (u^*, v^*)$  can be written as follows:

$$\mathbf{u}^* = \frac{\kappa^*}{\mu^*} [-\nabla^* \hat{p}^* + (\rho^* - \rho_0^*) \mathbf{g}^* + \rho_0^* \mathbf{g}^*], \quad (1)$$

where  $\rho_0^*$  is the reference bulk density usually taken as the bulk density of the host phase and  $\hat{p}^*$  is pressure. Considering an isotropic medium and a pressure decomposition such as  $\hat{p}^* = p^* + p_H^*$  with components  $p^*$  representing the reduced pressure, or pressure deviation, and  $p_H^*$  as the hydrostatic pressure, one can define  $\nabla^* p_H^* = \rho_0^* \mathbf{g}^*$ , and, therefore, the velocity  $\mathbf{u}^*$  is given by

$$\mathbf{u}^* = \frac{\kappa^*}{\mu^*} (-\nabla^* p^* + \Delta \rho^* \mathbf{g}^*), \quad (2)$$

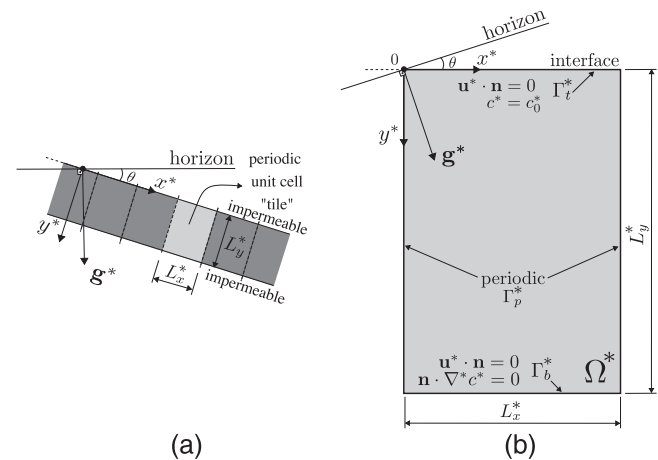


**FIG. 1.** Schematic diagram of the numerical domain  $\Omega^*$  with an interface inclined by an angle  $\theta$  with respect to the horizon. (a) A representative sketch of a possible physical large domain highlighting the unit cell employed in the numerical approach. (b) Detail of a periodic unit cell tile. Boundary conditions are shown for the velocity  $\mathbf{u}^*$  and concentration  $c^*$  of the dissolving solute at the bottom  $\Gamma_b^*$  and top  $\Gamma_t^*$ . Periodic boundary conditions are applied to the sidewalls  $\Gamma_p^*$ . Note that gravity is inclined with respect to the chosen reference frame and the  $z$  axis is pointing into the page, therefore positive vorticity is clockwise.

where  $\kappa^*$  is the permeability of the porous medium and  $\Delta\rho^* = \rho^* - \rho_0^* = \rho_0^* \alpha_c^* c^*$ . The solutal expansion coefficient of the solute is  $\alpha_c^* = (1/\rho_0^*) \partial\rho^*/\partial c^*$ . Hence, the Darcy law takes the form

$$\mathbf{u}^* = \frac{\kappa^*}{\mu^*} (-\nabla^* p^* + \rho_0^* \alpha_c^* c^* \mathbf{g}^*). \tag{3}$$

Considering the incompressibility condition and the concentration transport equation, the dimensional equations can now be written as follows:

$$\nabla^* \cdot \mathbf{u}^* = 0, \tag{4}$$

$$\nabla^* p^* = -\frac{\mu}{\kappa} \mathbf{u}^* + \rho_0^* \alpha_c^* c^* \mathbf{g}^*, \tag{5}$$

$$\phi \frac{\partial^* c^*}{\partial t^*} + (\mathbf{u}^* \cdot \nabla^*) c^* = \phi D^* \nabla^{*2} c^*, \tag{6}$$

where  $\phi$  is the porosity of the porous medium and  $D^*$  is the diffusion coefficient of the solute. The dimensionless form of Eqs. (4)–(6) can be found by choosing the pressure, hydrodynamic velocity, time, and length scales according to Ref. 11 as given by

$$p_c^* = \frac{\mu^* D^* \phi}{\kappa^*}, \quad u_c^* = \frac{\Delta\rho_0^* g^* \kappa^*}{\mu^*}, \quad t_c^* = \frac{\phi^2 D^*}{u_c^{*2}}, \quad l_c^* = \frac{\phi D^*}{u_c^*}. \tag{7}$$

The solubility  $c_0$  of the solute in the host phase is used as the characteristic concentration, and  $\Delta\rho_0^* = \rho_0^* \alpha_c^* c_0^*$ . Defining  $\mathbf{u} = \mathbf{u}^*/u_c^*$ ,  $\mathbf{g} = \mathbf{g}^*/g^*$ ,  $c = c^*/c_0^*$ ,  $y = y^*/l_c^*$ ,  $t = t^*/t_c^*$ , and  $\rho = (\rho^* - \rho_0^*)/\Delta\rho_0^*$ , the dimensionless equations are finally written using the definition of the material derivative  $Dc/Dt$  as

$$\nabla \cdot \mathbf{u} = 0, \tag{8}$$

$$\mathbf{u} = -\nabla p + c\mathbf{g}, \tag{9}$$

$$\frac{Dc}{Dt} = \nabla^2 c. \tag{10}$$

Considering a two-dimensional flow in the  $x - y$  plane, the vorticity field  $\boldsymbol{\omega} = \nabla \times \mathbf{u}$ , in general, has a nonzero  $z$ -component,  $\omega_z$ , a function of the concentration gradient and of the inclination angle  $\theta$ ,

$$\omega_z = \frac{\partial v}{\partial x} - \frac{\partial u}{\partial y} = \cos\theta \frac{\partial c}{\partial x} - \sin\theta \frac{\partial c}{\partial y}. \tag{11}$$

The dimensionless equations describing the dynamics in the flow field governing the evolution of the concentration field  $c$  close to the inclined surface are complete with the definition of the Poisson equation for the stream function  $\psi$  and the transport of the solute  $c$  as follows:

$$\nabla^2 \psi = -\left( \cos\theta \frac{\partial c}{\partial x} - \sin\theta \frac{\partial c}{\partial y} \right), \tag{12}$$

$$\frac{Dc}{Dt} = \nabla^2 c, \tag{13}$$

where  $\psi$  is the dimensionless stream function [ $\mathbf{u} = (u, v) = (\partial\psi/\partial y, -\partial\psi/\partial x)$ ]. Equation (12) is the vorticity equation with

Darcy law and Boussinesq approximation, and Eq. (13) is the concentration transport equation.

The simplifications adopted in this work, such as two-dimensional flow, isotropic, and homogeneous porous media, may bear important consequences in the system dynamics, and the present results may considerably vary if changes in these properties of the medium are taken into account. For instance, the anisotropy could change substantially the onset time and the dissolution rate at the convective regime, as shown in Paoli *et al.*,<sup>35</sup> for the horizontal case  $\theta = 0$ .

### A. Boundary conditions

To complete the definition of the problem, appropriate boundary and initial conditions need to be specified. The proposed mathematical problem is a model problem, where a very long (infinite) tilted layer of a porous medium is limited by two parallel non-deformable impermeable surfaces, as shown in Fig. 1(a). The parallel impermeable surfaces are considered to be planar and very large (infinite). We further simplify the problem considering a representative length in the downslope  $x$ -direction,  $L_x$ , and the analysis is performed on this representative periodic (finite) domain. On the edges of this representative domain, the Periodic Boundary Conditions (PBCs) are applied. PBCs are often chosen to approximate a large (infinite) domain by using a small part, or tile, called a unit cell, in computer simulations and mathematical models of physical problems in infinite domains, such as homogeneous turbulent and porous media flows.<sup>36–39</sup>

Boundary conditions are analogous to the case of the flat and horizontal interface, with null normal component of the velocity ( $v$ ) at the interface ( $\Gamma_t : y = 0$ ) and at the bottom ( $\Gamma_b : y = L_y$ ), and periodic boundary conditions at the sides ( $\Gamma_p : x = 0$  and  $x = L_x$ ). For concentration, boundary conditions are  $c(x, y) = 1 \mid (x, y) \in \Gamma_t$ ,  $\mathbf{n} \cdot \nabla c = 0 \mid (x, y) \in \Gamma_b$ , and periodic boundary conditions are used at the sides ( $\Gamma_p : x = 0$  and  $x = L_x$ ). The corresponding boundary conditions for the stream function are  $\psi = 0$  at the top ( $\Gamma_t$ ) and at the bottom ( $\Gamma_b$ ) interfaces, and periodic boundary conditions at the sides ( $\Gamma_p$ ). Thus, we are assuming null average flow rate. No explicit boundary conditions for the vorticity are required.

The only two nondimensional parameters of the problem are  $L_x$  and  $L_y$ . The parameter  $L_y$  can be properly identified as the (concentration–diffusion) Rayleigh–Darcy number,

$$\mathcal{R}a_y = L_y = \frac{L_y^* K g \Delta\rho}{\mu \phi D^*}, \tag{14}$$

which can be interpreted as the ratio between the concentration boundary layer thickness at unit time and the thickness of the porous slab.

Analogously, the nondimensional width,  $L_x$ , can be defined as

$$\mathcal{R}a_x = L_x = \frac{L_x^* K g \Delta\rho}{\mu \phi D^*}. \tag{15}$$

It can be noted that the problem may be described equivalently by the Rayleigh number  $\mathcal{R}a_y$  and the aspect ratio  $a_r$ ,

$$a_r = \frac{L_x^*}{L_y^*} = \frac{\mathcal{R}a_x}{\mathcal{R}a_y}. \tag{16}$$

As in the present analysis, the imposition of periodic boundary conditions is, in effect, simulating a narrow porous slab which is tilted at an angle to the vertical, the width  $L_x$  must be sufficiently long to contain a number of fingers which allows for the computation of meaningful average profiles. Appropriate initial conditions are also required and are defined as  $u, v, \omega, c = 0$  in  $\Omega$  and  $c(x, y, t = 0) = 1 + 2(\xi - 1/2) \times 10^{-3}$  at the interface ( $\Gamma_I$ ), where  $\xi$  is a random number in the range  $[0, 1]$ .

### III. BASE STATE SOLUTION

The base state of the problem, here denoted by  $\bar{c}, \bar{u}$ , and  $\bar{v}$ , is the time dependent solution of Eqs. (12) and (13) of the hydrodynamic and concentration fields, in the absence of perturbations and considering that the domain is infinite in the  $x$ -direction. This is equivalent to a *fully developed* assumption for the base flow and base concentration field in the  $x$ -direction, which implies that the base state satisfies  $\partial\bar{c}/\partial x = 0, \partial\bar{u}/\partial x = 0$ , and  $\partial\bar{v}/\partial x = 0$ . This is consistent with an infinite slab in the  $x$ -direction, thus reducing the base state to a one-dimensional, transient problem. Hence, our analysis is restricted to the case of a developed flow, “infinite domain,” or far from the edges of a very long domain.

The base state satisfies the continuity equation, therefore,

$$\frac{\partial\bar{v}}{\partial y} = -\frac{\partial\bar{u}}{\partial x} = 0. \tag{17}$$

Hence,  $\bar{v} = \bar{v}_0$  is a constant. Considering that the boundary condition at the upper surface is null normal component of the velocity, the  $y$ -component of the velocity of the base state is null,  $\bar{v} = 0$ . The convective terms in the concentration transport equation are

$$\bar{\mathbf{u}} \cdot \nabla\bar{c} = \bar{u} \frac{\partial\bar{c}}{\partial x} + \bar{v} \frac{\partial\bar{c}}{\partial y}. \tag{18}$$

Considering that the base state velocity has no component in the  $y$ -direction ( $\bar{v} = 0$ ), as shown above, and that the base concentration profile is not a function of  $x$  ( $\partial\bar{u}/\partial x = 0$ ), as assumed by the infinite slab hypothesis, therefore canceling the advection nonlinear terms, the concentration must satisfy the equation

$$\frac{\partial\bar{c}}{\partial t} = \frac{\partial^2\bar{c}}{\partial x^2} + \frac{\partial^2\bar{c}}{\partial y^2}. \tag{19}$$

Again, considering that  $\partial\bar{c}/\partial x = 0$ , the first term on the right-hand side of Eq. (19) vanishes, and the base state concentration field must satisfy

$$\frac{\partial\bar{c}}{\partial t} = \frac{\partial^2\bar{c}}{\partial y^2}. \tag{20}$$

#### A. Infinite Rayleigh number ( $\mathcal{Ra}_y \rightarrow \infty$ )

In the case of short times or very thick slabs, the domain can be considered semi-infinite in the  $y$  direction, and the appropriate boundary conditions are

$$\bar{c}(y = 0, t) = 1, \tag{21}$$

$$\bar{c}(y \rightarrow \infty, t) = 0, \tag{22}$$

and initial conditions

$$\bar{c}(y = 0, t = 0) = 1, \tag{23}$$

$$\bar{c}(y > 0, t = 0) = 0. \tag{24}$$

The solution of Eq. (20), subject to boundary conditions Eqs. (21) and (22) and initial conditions Eqs. (23) and (24), is given by

$$\bar{c}(y, t) = 1 - \operatorname{erf}\left(\frac{y}{2\sqrt{t}}\right). \tag{25}$$

Thus, the diffusive transient base concentration profile  $\bar{c}(y, t)$  is not affected by the inclination of the slab and is identical to the classical horizontal slab ( $\theta = 0$ ), regardless of the slab inclination angle  $\theta$ . The base velocity can be obtained from either Eq. (9) or from the stream-function equation (12). Using this last approach,

$$\frac{\partial^2\bar{\psi}}{\partial y^2} = \sin\theta \frac{\partial\bar{c}}{\partial y}. \tag{26}$$

Hence,

$$\frac{\partial\bar{\psi}}{\partial y} = \bar{u}(y, t) = \sin\theta \bar{c}(y, t) + f(x). \tag{27}$$

Using the condition that  $\partial\bar{u}/\partial x = 0, f(x) = \bar{u}_0$ , an arbitrary constant. Therefore, the  $x$ -velocity component is given by

$$\bar{u}(y, t) = \sin\theta \left[ 1 - \operatorname{erf}\left(\frac{y}{2\sqrt{t}}\right) \right] + \bar{u}_0. \tag{28}$$

Without loss of generality, the constant  $\bar{u}_0$ , corresponding to the average flow across the slab, can be chosen as null or any arbitrarily value, depending on the desired problem of interest. For instance, if an average velocity  $\bar{u}_A$  is specified,

$$\bar{u}_A = \frac{1}{L_y} \int_0^{L_y} \left( \sin\theta \left[ 1 - \operatorname{erf}\left(\frac{y}{2\sqrt{t}}\right) \right] + \bar{u}_0 \right) dy; \tag{29}$$

therefore,

$$\bar{u}_0 = \bar{u}_A - \frac{1}{L_y} \int_0^{L_y} \sin\theta \left[ 1 - \operatorname{erf}\left(\frac{y}{2\sqrt{t}}\right) \right] dy. \tag{30}$$

In general, taking  $\bar{u}_0 = 0$  introduces a small average mass flux across the slab that is negligible in the case of small diffusive times or large values of  $L_y$ . Two different solutions, corresponding to different values of  $\bar{u}_A$ , can be interpreted as the same solution viewed from moving frames with different velocities. Choosing the solution with  $\bar{u}_A = 0$  is consistent, for instance, with the case of a very long slab with one or both of the (far away) edges closed by impermeable walls, as viewed from an observer not moving with respect to the slab.

On the other hand, choosing a constant average background velocity in the layer as the solution with  $\bar{u}_A = C_A$ , where  $C_A$  is an arbitrary constant, is consistent with the same previous problem viewed by an observer with velocity  $\bar{u}_{\text{observer}} = -C_A$ , or with an observer with  $\bar{u}_{\text{observer}} = 0$ , but for a problem where there is a net flow rate corresponding to an average velocity  $\bar{u}_A = C_A$ . Hence, the same mathematical problem and its respective solution can be

interpreted as different physical phenomena, just by applying a simple change of variables, and the corresponding change in average pressure gradient. Indeed, adding or subtracting an arbitrary velocity represents different physical phenomena, that a linear Darcy’s model may not be appropriate to describe.

For simplicity, in the linear stability analysis, for infinite  $\mathcal{Ra}_y$ , we will consider that  $L_y \rightarrow \infty$ ; hence,  $\bar{u}_0 = 0$ .

There is thus a base drift velocity  $\bar{u}$  induced by the base concentration profile that increases with the inclination angle  $\theta$ . Therefore, the  $x$ -velocity component is given by

$$\bar{u}(y, t) = \sin \theta \left[ 1 - \operatorname{erf} \left( \frac{y}{2\sqrt{t}} \right) \right]. \quad (31)$$

It can be observed that the base states  $\bar{c}$ ,  $\bar{u}$ , and  $\bar{v}$ , here obtained for a semi-infinite domain in the  $y$  direction, are consistent with the boundary conditions of the periodic “tile” that were described in Sec. II A. Furthermore, the base state solutions given by either Eq. (28) or Eq. (31) imply that, for  $\theta \neq 0$ , there is always a nonzero base velocity, and the no-flow is an impossible condition.

### B. Finite Rayleigh number ( $\mathcal{Ra}_y \ll 4\sqrt{t}$ )

In case of longer times, or thin slabs, the domain cannot be considered semi-infinite in the  $y$  direction, and the appropriate boundary conditions are

$$\bar{c}(y = 0, t) = 1, \quad (32)$$

$$\frac{\partial \bar{c}}{\partial y}(y = \mathcal{Ra}_y, t) = 0, \quad (33)$$

and initial conditions,

$$\bar{c}(y = 0, t = 0) = 1, \quad (34)$$

$$\bar{c}(y > 0, t = 0) = 0. \quad (35)$$

The solution of Eq. (20), subject to boundary conditions Eqs. (32) and (33) and initial conditions Eqs. (34) and (35), is given by<sup>17</sup>

$$\bar{c}(y, t) = 1 + \sum_{n=1}^{\infty} \frac{4}{(2n-1)\pi} e^{-[(2n-1)\pi/(2\mathcal{Ra}_y)]^2 t} \sin \left( \frac{2n-1}{2\mathcal{Ra}_y} \pi y \right) \quad (36)$$

and

$$\bar{u}(y, t) = \bar{c} \sin \theta + \bar{u}_0, \quad (37)$$

where the same arguments regarding  $\bar{u}_0$  also apply. As mentioned in Ref. 17, Eq. (25) is a good approximation of Eq. (36), as long as  $\mathcal{Ra}_y \geq 4\sqrt{t}$ .

Once the cell is tilted, the critical porous Rayleigh number for convection is zero, in the sense that there is always flow in the base state, as shown in Eq. (37). Previous studies, for example, Weber,<sup>40</sup> Sen *et al.*<sup>41</sup> and Moya *et al.*,<sup>42</sup> have addressed the base state flow for tilted rectangular porous material. Moya *et al.*<sup>42</sup> considered a rectangular domain with isothermal boundary conditions on two opposite sides and the other two are thermally insulated (a finite “two-sided” system) and found that the earliest mode of convection is that of a

recirculating flow. For large aspect ratios, this takes the form of a countercurrent exchange flow. In the present work, considering a very large (infinite) aspect ratio and transient “one-sided” system, a comparable base state is also found.

The base state may or may not be a stable solution with regard to small perturbations, and, therefore, may not be always observable in actual physical situations. The question of the base state stability with regard to small perturbations will be addressed in Sec. IV.

## IV. LINEAR STABILITY ANALYSIS OF THE BASE STATE

### A. LSA formulation

The linear stability analysis (LSA) consists in adding perturbations to the base state solution characterized by the concentration and hydrodynamic profiles [Eqs. (25) and (31)] as

$$\begin{pmatrix} c \\ \psi \end{pmatrix} = \begin{pmatrix} \bar{c} \\ \bar{\psi} \end{pmatrix}(y, t) + \begin{pmatrix} \tilde{c} \\ i\tilde{\psi} \\ k \end{pmatrix}(y) \exp(\sigma t + ikx), \quad (38)$$

where  $i^2 = -1$ ,  $k$  is the wavenumber of the perturbation, and  $\sigma$  is the growth rate. The current approximation considers a sequence of quasi-steady states (as has been considered in numerous previous examples) and is similar to the approach taken by Riaz *et al.*<sup>21</sup> More sophisticated approaches have recently been used, which perturb the self-similar diffusive base state using the self-similar variables (Slim and Ramakrishnan<sup>17</sup> or Nijjer *et al.*<sup>38</sup>). The linearized evolution equations for the disturbances  $\tilde{c}$  and  $\tilde{\psi}$ , considering that the base state evolution is much slower than the perturbation growth, are, thus,

$$\tilde{\psi}_{yy} - k^2 \tilde{\psi} = -(k^2 \cos \theta \tilde{c} + ik \sin \theta \tilde{c}_y), \quad (39)$$

$$\sigma \tilde{c} + \tilde{c}_y \tilde{\psi} + ik \tilde{u} \tilde{c} = \tilde{c}_{yy} - k^2 \tilde{c}. \quad (40)$$

Boundary conditions for the concentration and stream-function perturbations  $\tilde{c}$  and  $\tilde{\psi}$  are

$$y = 0: \quad \tilde{c} = 0, \quad \tilde{\psi} = 0, \quad (41)$$

$$y \rightarrow \infty: \quad \tilde{c} \rightarrow 0, \quad \tilde{\psi} \rightarrow 0 \quad (42)$$

for semi-infinite domains or

$$y = 0: \quad \tilde{c} = 0, \quad \tilde{\psi} = 0, \quad (43)$$

$$y = L_y: \quad \frac{d\tilde{c}}{dy} = 0, \quad \tilde{\psi} = 0 \quad (44)$$

for finite domains.

Upon defining  $D^n = d^n/dy^n$ , we rewrite Eq. (39) as

$$(D^2 - k^2) \tilde{\psi} = -(k^2 \cos \theta \tilde{c} + ik \sin \theta D\tilde{c}), \quad (45)$$

and inversely,

$$\tilde{\psi} = -(D^2 - k^2)^{-1} (k^2 \cos \theta \tilde{c} + ik \sin \theta D\tilde{c}). \quad (46)$$

Likewise, Eq. (40) is rewritten as

$$\sigma \tilde{c} + \tilde{c}_y \tilde{\psi} + ik \tilde{u} \tilde{c} = (D^2 - k^2) \tilde{c}. \quad (47)$$

Upon replacing  $\tilde{\psi}$  from Eq. (46) in Eq. (47) and rearranging terms, we arrive at the equation

$$\left[ ik\bar{u} - \bar{c}_y (D^2 - k^2)^{-1} (k^2 \cos \theta + ik \sin \theta D) - (D^2 - k^2) \right] \tilde{c} = -\sigma \tilde{c}, \tag{48}$$

or using Eq. (27),

$$\left\{ \left[ -ik \sin \theta \bar{c} + \bar{c}_y (D^2 - k^2)^{-1} (k^2 \cos \theta + ik \sin \theta D) \right] + (D^2 - k^2) \right\} \tilde{c} = \sigma \tilde{c}. \tag{49}$$

Equation (49) is an eigenvalue–eigenfunction problem to find pairs  $(\sigma, \tilde{c})$ , for each value of  $\theta, k$  and a given  $t$ , which defines  $\bar{c}$ . The most unstable mode corresponds to the eigenfunction with the eigenvalue of greatest *real* part,  $\sigma_R$ . The phase velocity of the perturbations is associated to the *imaginary* part of the eigenvalue,  $\sigma_I$ , by  $v_p = -\sigma_I/k$ . Hence, the angular frequency is  $-\sigma_I$ .

Considering the base state solution obtained from Eqs. (20) and (27) for a given time, a LSA can be performed using Eq. (49) to obtain dispersion curves giving the growth rate of the perturbations, as well as the drift velocity, as a function of the wavenumber.

### B. Discretization of the linearized equations

The eigenvalue problem in Eq. (49) is solved using the Chebyshev spectral collocation method<sup>39,43,44</sup> where the solution of the differential equation and its boundary conditions are expanded as a finite series in the Chebyshev polynomials of the form

$$\phi(\zeta) \approx \phi_N(\zeta_j) = \sum_{k=0}^N \hat{\phi}_k T_k(\zeta_j), \quad j = 0, 1, \dots, N, \tag{50}$$

$$T_0(\zeta) = 1, \quad T_1(\zeta) = \zeta, \quad T_{k+1}(\zeta) - 2\zeta T_k(\zeta) + T_{k-1}(\zeta) = 0, \tag{51}$$

where  $\hat{\phi}_k$  represents the unknown coefficients and  $\zeta_j$  are the collocation points.<sup>45</sup>

For finite domains, we employ the Chebyshev–Gauss–Lobatto (CGL) collocation points on the interval  $[-1, 1]$  defined by

$$\zeta_j = \cos(j\pi/N), \quad j = 0, 1, \dots, N. \tag{52}$$

The CGL interpolation derivative  $w$  of a function  $h$  can be represented in matrix form as

$$w = \frac{dv}{d\zeta} = D_N h. \tag{53}$$

The entries  $(D_N)_{ij}$  can be computed by differentiating the characteristic Lagrange polynomials  $L_i(\zeta)$  of degree  $N$ , which are 1 at  $\zeta_i$

and 0 at all the other collocation points, and are given by

$$(D_N)_{00} = \frac{2n^2 + 1}{6}, \tag{54}$$

$$(D_N)_{NN} = -\frac{2n^2 + 1}{6}, \tag{55}$$

$$(D_N)_{jj} = \frac{-\zeta_j}{2(1 - \zeta_j^2)}, \quad j = 1, \dots, N - 1, \tag{56}$$

$$(D_N)_{ij} = \frac{c_i (-1)^{i+j}}{c_j \zeta_i - \zeta_j}, \quad i \neq j, \quad \text{and } i, j = 1, \dots, N, \tag{57}$$

where

$$c_i = \begin{cases} 2, & i = 0 \text{ or } N, \\ 1, & \text{otherwise.} \end{cases} \tag{58}$$

The CGL collocation points are mapped to the required domain using a smooth monotonic transformation map  $\phi_M$ .<sup>46–48</sup> For infinite domains, the linear map  $\phi_L$  is employed,

$$y = \phi_L(\zeta) = \frac{L_y}{2}(1 + \zeta), \tag{59}$$

where  $L_y$  is the domain size in the  $y$  direction.

For semi-infinite domains, the Chebyshev–Gauss–Radau (CGR) collocation points<sup>49</sup> on the interval  $[-1, 1)$  are defined by

$$\zeta_j = \cos(2j\pi/(2N + 1)), \quad j = 0, 1, \dots, N. \tag{60}$$

The entries  $(D_N)_{ij}$  are given by

$$(D_N)_{00} = \frac{(n + 1)n}{3}, \tag{61}$$

$$(D_N)_{jj} = -\frac{1}{2(1 - \zeta_j^2)}, \quad j = 1, \dots, N, \tag{62}$$

$$(D_N)_{ij} = \frac{c_i (-1)^{i+j}}{c_j \zeta_i - \zeta_j}, \quad i \neq j \quad \text{and } i, j = 1, \dots, N, \tag{63}$$

where

$$c_i = \begin{cases} 2, & i = 0, \\ \sqrt{\frac{2}{1 + \zeta_i}}, & \text{otherwise.} \end{cases} \tag{64}$$

and the algebraic map onto a half-open interval  $\phi_A : y \in [0, \infty) \rightarrow \zeta \in [-1, 1)$  is defined as

$$y = \phi_A(\zeta) = L_A \frac{1 + \zeta}{1 - \zeta}. \tag{65}$$

The value of the constant  $L_A = 1 \times 10^5$  is chosen such that the mapping produces the smallest error over the range of interest.

Substituting Eq. (53) into Eq. (49), requiring that it be satisfied at the  $N - 1$  internal collocation points, and applying the appropriate conditions at the two boundaries, we obtain  $(N + 1) \times (N + 1)$  algebraic equations that form the discrete eigenvalue problem,

$$M\tilde{c} = \sigma \tilde{c}. \tag{66}$$

Here,  $M$  is the discrete analog of the left-hand side (LHS) operator in Eq. (49). The eigenvalue  $\sigma_M$ , with largest real part,

corresponds to the most unstable mode, which is the most relevant one. The algorithm was implemented in Julia Programming Language, which provides multithreading for computational performance. We employed  $N + 1 = 1024$  collocation points, and three domain lengths:  $L_y \rightarrow \infty$  to represent a semi-infinite layer,  $L_y = 12\,000$  to represent a deep slab, and the case of  $L_y = 3000$  to illustrate the effect of a shallow slab at long times. Results are presented in Sec. IV C.

### C. LSA results

#### 1. Infinite $\mathcal{R}a_y$

In the case of infinite  $\mathcal{R}a_y$ , Fig. 2 shows the dispersion curves of normal mode perturbations of the base state, numerically obtained for several times, in the case of an horizontal interface [ $\theta = 0$ —see Fig. 2(a), solid lines] compared to one inclined interface case [ $\theta = \pi/16$ —see Fig. 2(b), dashed lines]. The real part of  $\sigma$  [Fig. 2(a)] shows the growth ( $\sigma_R > 0$ ) or decay ( $\sigma_R < 0$ ) rate of the perturbations.

Figure 2(a) shows results for  $\theta = 0$  that reproduce previous works.<sup>11</sup> In this case, it can be seen that all perturbations are damped for  $t < 55.59$ . A first perturbation becomes marginally stable ( $\sigma_R = 0$ ) with a wavenumber  $k = 0.0583$ , at  $t = 55.59$  (solid green curve). The characteristic time  $t_c$  and the respective growth rate  $\sigma_{Rc}$  are defined as the smallest time and growth rate for which  $\sigma_{Rc}t_c > 1$ , such that the amplification factor  $\exp(\sigma_{Rc}t_c)$  of the perturbation at the characteristic  $t_c$  is of order unity, as performed by Trevelyan *et al.*<sup>50</sup> and others.<sup>11</sup> From this definition, we find the

following characteristic values:  $\sigma_{Rc} = 3.96 \times 10^{-3}$ ,  $t_c = 252.86$ , and  $k = 6.192 \times 10^{-2}$ .

For the case of the inclined interface,  $\theta > 0$ , all curves are displaced to the left and downward, showing an increase in the stability of the flow, reducing the maximum growth rate and the maximum amplified wavenumber. Figure 2(b) shows the effect of the inclination on the phase velocity  $v_p = -\sigma_I/k$ . It can be seen that for the horizontal interface,  $\theta = 0$ , the perturbations have zero phase velocity. On the other hand, for the inclined interface,  $\theta = \pi/16$ , the perturbation phase velocity is positive and increases with wavenumber  $k$  and time  $t$ .

The dispersion curves for various angles of inclination at  $t = 252.86$  are shown in Fig. 3. The effect of the inclination can be seen to gradually decrease the maximum amplification, the wavenumber of maximum amplification, and the maximum amplified wavenumber as the inclination angle increases. For  $\theta > 5\pi/31$ , perturbations of all wavenumbers are attenuated. A very clear effect of the inclination can also be seen on the imaginary part of the eigenvalue, which gives rise to the drift velocity of the perturbations [Fig. 3(b)]. For  $\theta = 0$ , the eigenvalue is real, and, therefore, there is no drift velocity. However, as  $\theta$  departs from zero,  $\sigma_I$  and the drift velocity,  $-\sigma_I/k$  increase. The phase velocity increases almost proportionally to the maximum base state velocity  $\bar{u}_{\max} = \sin \theta$ ; hence, the curves for various interface inclination angles almost coincide when the phase velocity is normalized by  $\sin \theta$ .

Figure 4 shows the results for large  $k$ . Figure 4(a) features the decay rate ( $-\sigma_R$ ) for different interface angles, showing that, for large  $k$ , all perturbations decay approximately at the same rate, regardless of the inclination angle. Figure 4(b) shows that the drift

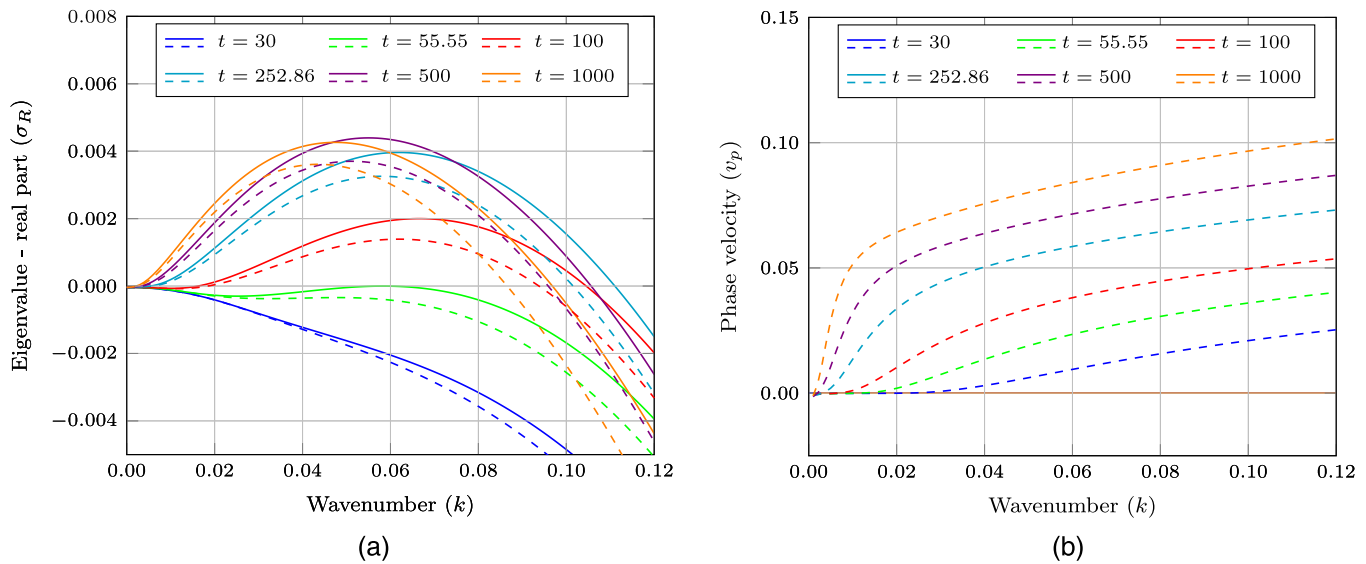


**FIG. 2.** (a) Dispersion curves giving the real part  $\sigma_R$  of normal mode perturbations of the base state as a function of their wavenumber  $k$  numerically obtained for several times. Solid lines,  $\theta = 0$ , dashed lines,  $\theta = \pi/16$ . For  $\theta = 0$ , all perturbations are damped for  $t < 55.59$ , and a bifurcation occurs at  $t = 55.59$  when the first perturbation becomes marginally stable with a wavenumber  $k = 0.0583$ . For  $\theta = \pi/16$ , all the curves are slightly displaced to the left and downward. (b) Dispersion curves showing the phase velocity,  $v_p = -\sigma_I/k$ , (imaginary part) of normal mode perturbations of the base state as a function of their wavenumber, numerically obtained for several times. Solid lines,  $\theta = 0$ , dashed lines,  $\theta = \pi/16$ . All perturbations are stationary for  $\theta = 0$ . For  $\theta = \pi/16$ , the perturbation phase velocity increases with wavenumber  $k$  and with time  $t$ .

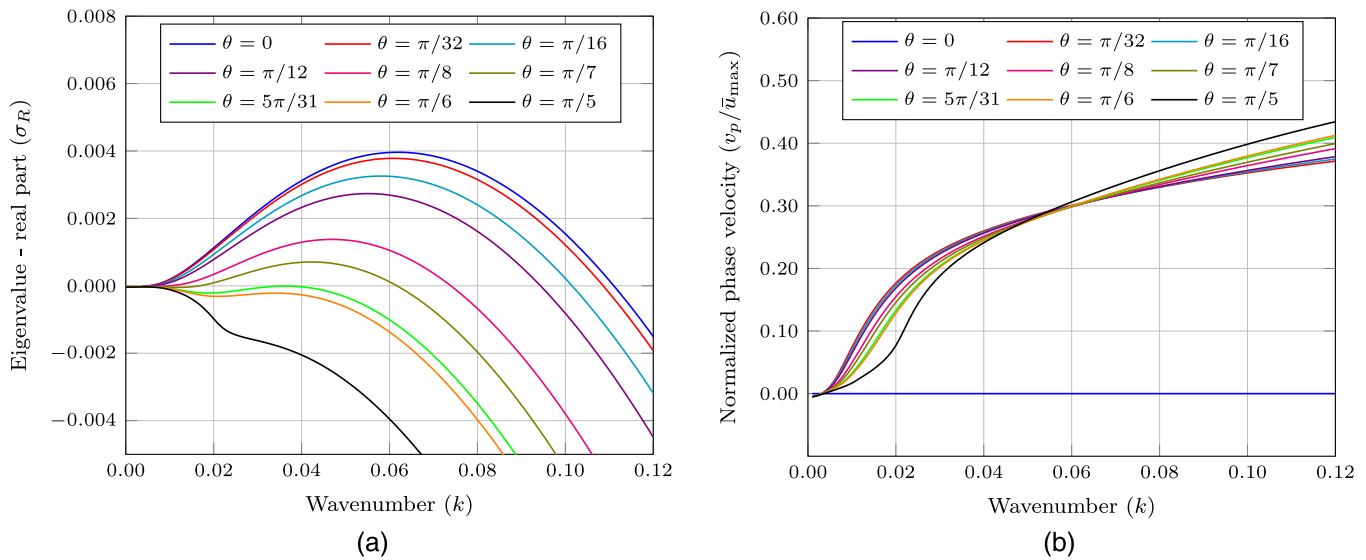


**FIG. 3.** (a) Dispersion curves giving the real part  $\sigma_R$  of normal mode perturbations as a function of their wavenumber  $k$  for several inclination angles  $\theta$  at  $t = 252.86$ . (b) Phase velocity of the perturbations normalized by the maximum base state velocity,  $v_p/\bar{u}_{max} = -\sigma_i/(k \cdot \sin \theta)$  as a function of the wavenumber obtained for several inclination angles  $\theta$  and  $t = 252.86$ . The perturbations are stationary for  $\theta = 0$ . For  $\theta > 0$ , the perturbation phase velocity increases with angle  $\theta$  and with wavenumber  $k$ ; hence, the normalized curves for various angles almost coincide.

velocity divided by  $\sin \theta$  approaches asymptotically the value 1, whatever the value of  $\theta$ . This result is expected since larger  $k$  modes are restricted to regions closer to the interface, where the nondimensional mean concentration is unitary, and the flow velocity is  $\sin \theta$ .

On the other hand, smaller  $k$  modes penetrate deeper away from the interface where the mean flow velocity is smaller.

Figure 5 shows the neutral stability curves ( $\sigma_R = 0$ ) in the  $k \times t$  plane of normal mode perturbations of the base state, numerically

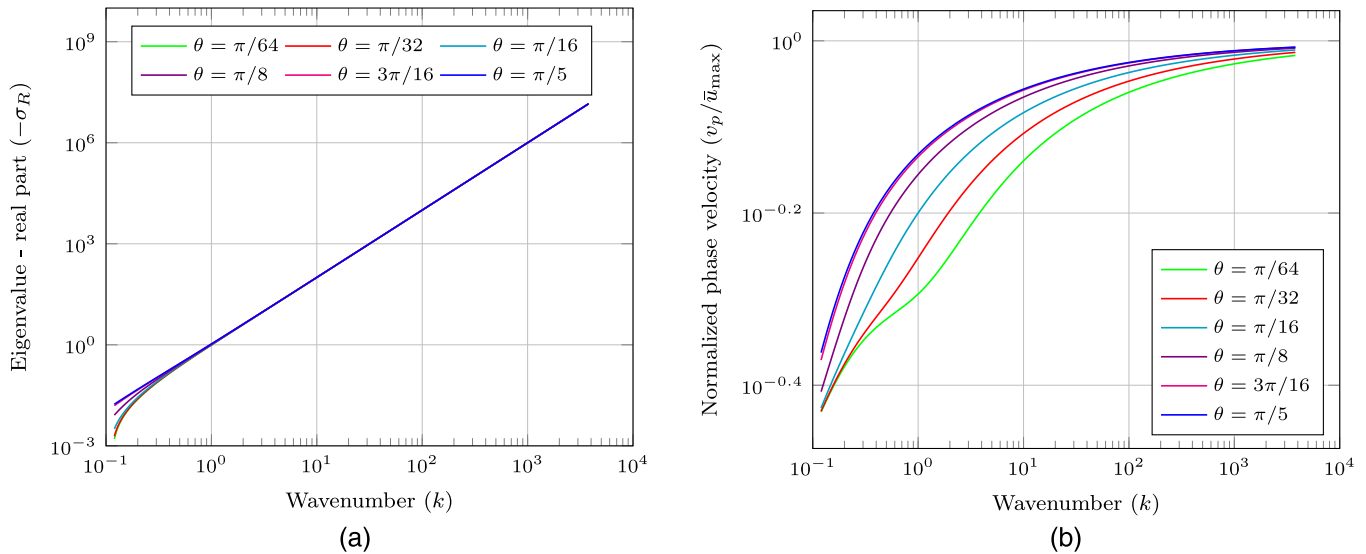


**FIG. 4.** Dispersion curves of normal mode perturbations of the base state, numerically obtained for several inclination angles  $\theta$  and  $t = 252.86$ , for large values of wavenumber  $k$ : (a) real part and (b) imaginary part—showing the phase velocity normalized by the maximum base state velocity,  $v_p/\bar{u}_{max}$ .

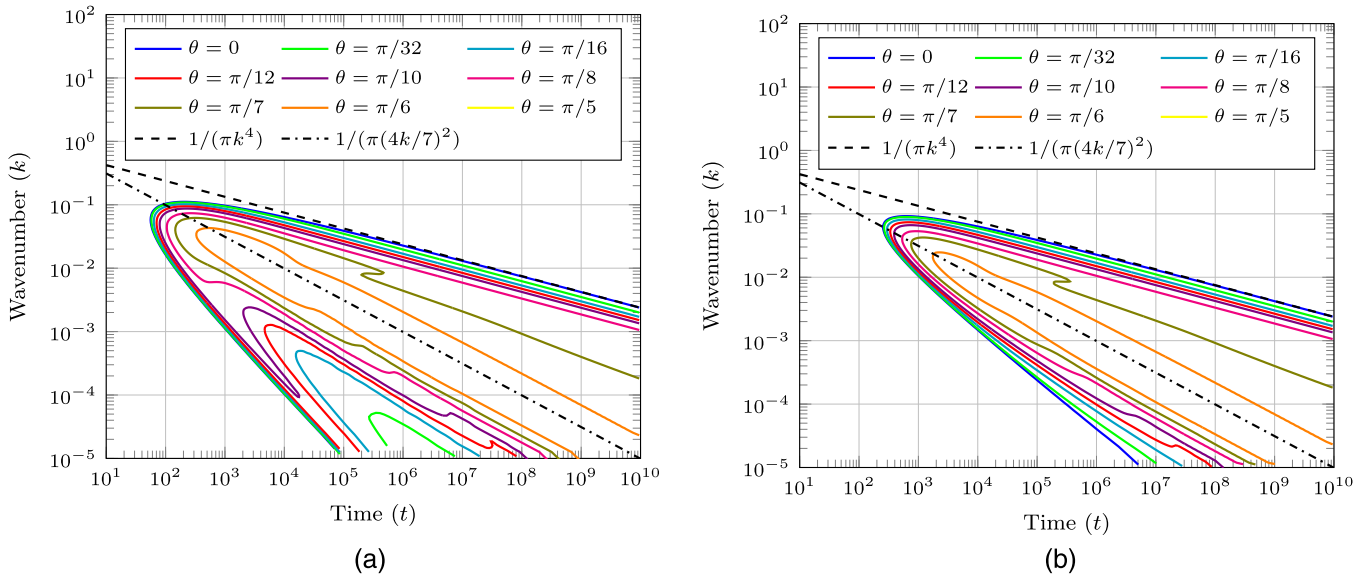


**FIG. 5.** (a) Neutral stability curves ( $\sigma_R = 0$ ) in the  $k \times t$  plane of normal mode perturbations of the base state, numerically obtained for several inclination angles  $\theta$ . The dashed line is the approximation  $t \approx 1/(\pi k^4)$  for the short-wave cut-off, as given by Slim and Ramakrishnan<sup>17</sup> for  $\theta = 0$ . For  $\theta \gtrsim \pi/6$ , the neutral stability curve collapses toward the approximate curve  $t \approx 1/(\pi(4k/7)^2)$  (dashed-dotted line) and disappears completely for  $\theta \gtrsim \pi/5$ . (b) Level contours of  $\sigma_R t = 1$ , as performed by Trevelyan *et al.*<sup>50</sup> and others,<sup>11</sup> showing that the lower branch of unstable modes seen for  $\sigma_R = 0$  (left) is dynamically not relevant. (a)  $\sigma_R = 0$ , (b)  $\sigma_R t = 1$ .

obtained for several inclination angles  $\theta$ . The results for  $\theta = 0$  are comparable to the results presented by Slim and Ramakrishnan<sup>17</sup> for the impermeable upper boundary case. The dashed line is the curve  $t \approx 1/(\pi k^4)$  that can be seen to approximate the limit of stability for the short-wave cut-off, as given by Slim and Ramakrishnan<sup>17</sup> for  $\theta = 0$ .

It can be observed that the curves are displaced to the right and downward as the angle is increased, getting progressively apart from the short-wave cut-off curve derived for  $\theta = 0$  [see in Fig. 5(a)]. Hence, the fingering instability is expected to occur at later times and with smaller wavenumbers as the angle is increased. Also, in general, as the inclination angle  $\theta$  is increased, there is a reduction on the range of wavenumbers with  $\sigma_R > 0$ , up to  $\theta = \pi/5$ , where no growing modes were observed. For angles close to  $\theta = \pi/12$ , a peculiar behavior is observed for times close to  $t = 5 \times 10^3$ , where two separate ranges of unstable wavenumbers are present. The slope of the upper limit of stability is increasingly steeper as  $\theta$  increases, until, for  $\theta \gtrsim \pi/6$ , the neutral stability curve collapses to the approximate curve  $t \approx 1/(\pi(4k/7)^2)$  [see dashed-dotted curve in Fig. 5(a)]. The physical reasoning on why the growth curves are non-monotonic at times  $10^3 < t < 10^4$  (for example), that is, why are there intermediate wavenumbers which are stable, while larger and smaller wavenumbers are unstable, will be addressed in Sec. IV D, that deals with the eigenmodes of the LSA. Figure 5(b) shows the level contours of  $\sigma_R t = 1$ , as performed by Trevelyan *et al.*<sup>50</sup> and others.<sup>11</sup> These curves are more representative of the dynamically relevant modes, which have a sufficiently large growth rate to actually become of finite amplitude and appear in a significant manner. It can be observed that, considering this

criterion, there are no significant modes on the lower branch seen in Fig. 5(a).

### 2. Finite Rayleigh number ( $\mathcal{Ra}_x$ and $\mathcal{Ra}_y$ ) effects

In the LSA,  $\mathcal{Ra}_x$  is given by a periodic unit cell with  $\mathcal{Ra}_x = 2\pi/k$ . When performing direct numerical simulations, it is necessary to keep a domain with at least  $L_x = \mathcal{Ra}_x \geq 2\pi/k$  to accurately capture the behavior of modes associated with wavenumber  $k$  and simulate a virtually infinite domain. We must stress that periodic conditions in direct numerical simulations cause mode restrictions, thus not reproducing an infinite domain for large wavelength perturbations.

The effect of finite  $\mathcal{Ra}_y$  is somewhat similar, in the sense that as the wavelength of the perturbation increases, so does the depth of the eigenmodes. The domain depth size  $L_y = \mathcal{Ra}_y \geq 2\pi/k$  for the domain to be considered “deep.” In case  $\mathcal{Ra}_y \ll \mathcal{Ra}_x$ , we will be analyzing a “shallow” domain. The effect of a finite depth domain is illustrated in Fig. 6, which reproduces the same results presented in Fig. 5(b), however, considering two shallow domains, with  $L_y = \mathcal{Ra}_y = 12\,000$  and  $L_y = \mathcal{Ra}_y = 3\,000$ . The comparison shows that long wave perturbations are more stable in the shallow domains than in the deep domains, and eventually all unstable modes tend to be suppressed for long times. The finite domains show a critical time after which no unstable perturbations are present considering the  $\sigma_R t > 1$  criterion, and this critical time is smaller for smaller  $\mathcal{Ra}_y$  numbers.

The effect of the inclination is not just equivalent to a system with effective Rayleigh number  $\mathcal{Ra}'_y = \mathcal{Ra}_y \cos \theta$ , but will

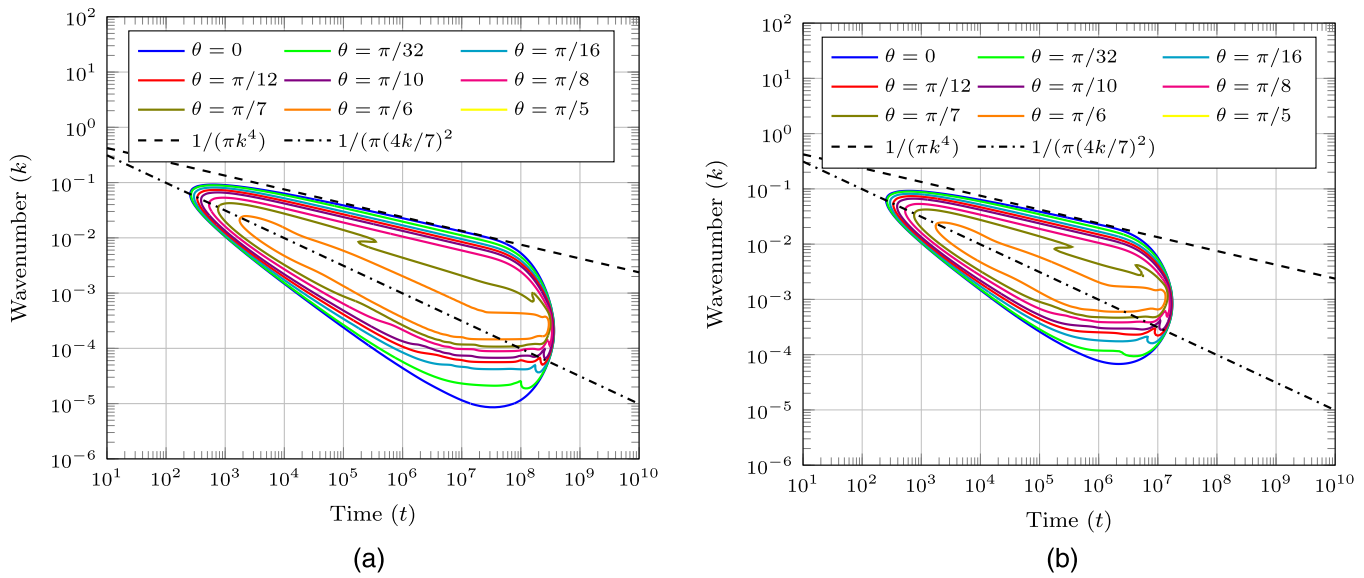


**FIG. 6.** Level contours ( $\sigma_R t = 1$ ) in the  $k \times t$  plane of normal mode perturbations of the base state, numerically obtained for several inclination angles  $\theta$ . The dashed line is the approximation  $t \approx 1/(\pi k^4)$  for the short-wave cut-off, as given by Slim and Ramakrishnan<sup>17</sup> for  $\theta = 0$ . For  $\theta \gtrsim \pi/6$ , the critical stability curve collapses toward the approximate curve  $t \approx 1/(\pi(4k/7)^2)$  (dashed-dotted line), and disappears completely for  $\theta \gtrsim \pi/5$ . (a) For  $\mathcal{R}a_y = 12000$ , the range of critically unstable modes decreases for large times until  $t > 4 \times 10^8$ , when no unstable wavenumbers are found. (b) For  $\mathcal{R}a_y = 3000$ , no critically unstable wavenumbers are found for  $t > 2 \times 10^7$ . (a)  $\mathcal{R}a_y = 12000$ , (b)  $\mathcal{R}a_y = 3000$ .

additionally suffer from the effect of the phase velocity caused by the combined effect of the gravity and the mean concentration profile. This can be observed, comparing Figs. 5(b) and 6 where the effect of the inclination is to reduce the range of unstable wavenumbers and delay the onset of the instability, while the main effect of the finite  $\mathcal{R}a_y$  is to suppress the unstable modes at long times.

**D. Eigenmodes analysis**

For each eigenvalue  $\sigma$  of the stability surface, there is a corresponding eigenmode  $(\tilde{c}, \tilde{\psi})$  that defines the physical effect of the perturbation. The analysis of some representative eigenmodes is important to understand some of the features obtained from the LSA.

The (real) space representation of the eigenmodes can be obtained from Eq. (38),

$$\begin{pmatrix} c' \\ \psi' \end{pmatrix} = \left[ \begin{pmatrix} \tilde{c} \\ i\tilde{\psi} \\ k \end{pmatrix} (y) \exp(\sigma t + ikx) \right] + C.C., \quad (67)$$

where *C.C.* stands for the complex conjugate of the expression between brackets. The amplitude and phase of the eigenmodes is arbitrary. However, the relationship between the amplitudes and phases of  $\tilde{c}$  and  $\tilde{\psi}$  is not and may help understand the underlying physics.

**1. Horizontal interface**

In the case of an horizontal interface, ( $\theta = 0$ ), the real space representations of the eigenmodes  $(c', \psi')$  are symmetric, due to the absence of any convection effect from the base state, as seen in Fig. 7.

For large  $k$  [i.e.,  $k = 5 \times 10^{-2}$ , Fig. 7 (first row)], the most unstable modes are restricted to the region of the base state concentration boundary layer, while for smaller values of  $k$  [i.e.,  $k = 1 \times 10^{-2}$ , Fig. 7 (second row), and  $k = 4 \times 10^{-4}$ , Fig. 7 (third row)] they extend to regions outside the boundary layer.

**2. Moderate inclination**

In the case of a moderately inclined interface ( $\theta = \pi/12$ ), the real space representations of the eigenmodes  $(c', \psi')$  are no longer symmetric, due to the presence of the convection effect from the base state, as seen in Fig. 8. The associated modes are tilted in the clockwise direction, with an inclination that varies with  $k$  with eigenmodes associated to  $k = 1.4 \times 10^{-3}$ , showing a stronger inclination (see Fig. 8—third row). The larger inclination of the modes may be associated to a relatively lower growth rate.

However, the inclination of the eigenmodes is not monotonically decreasing with  $k$ , showing that for intermediate values (i.e.,  $k = 1.4 \times 10^{-3}$ , Fig. 8—third row) the inclination is higher than for lower values (i.e.,  $k = 4.0 \times 10^{-4}$ , Fig. 8—fourth row). This non-monotonic dependence of the inclination of the eigenmodes can be related and give a possible explanation for the non-monotonic behavior of the stability surface ( $\sigma_R(t, k)$ ) on this region.

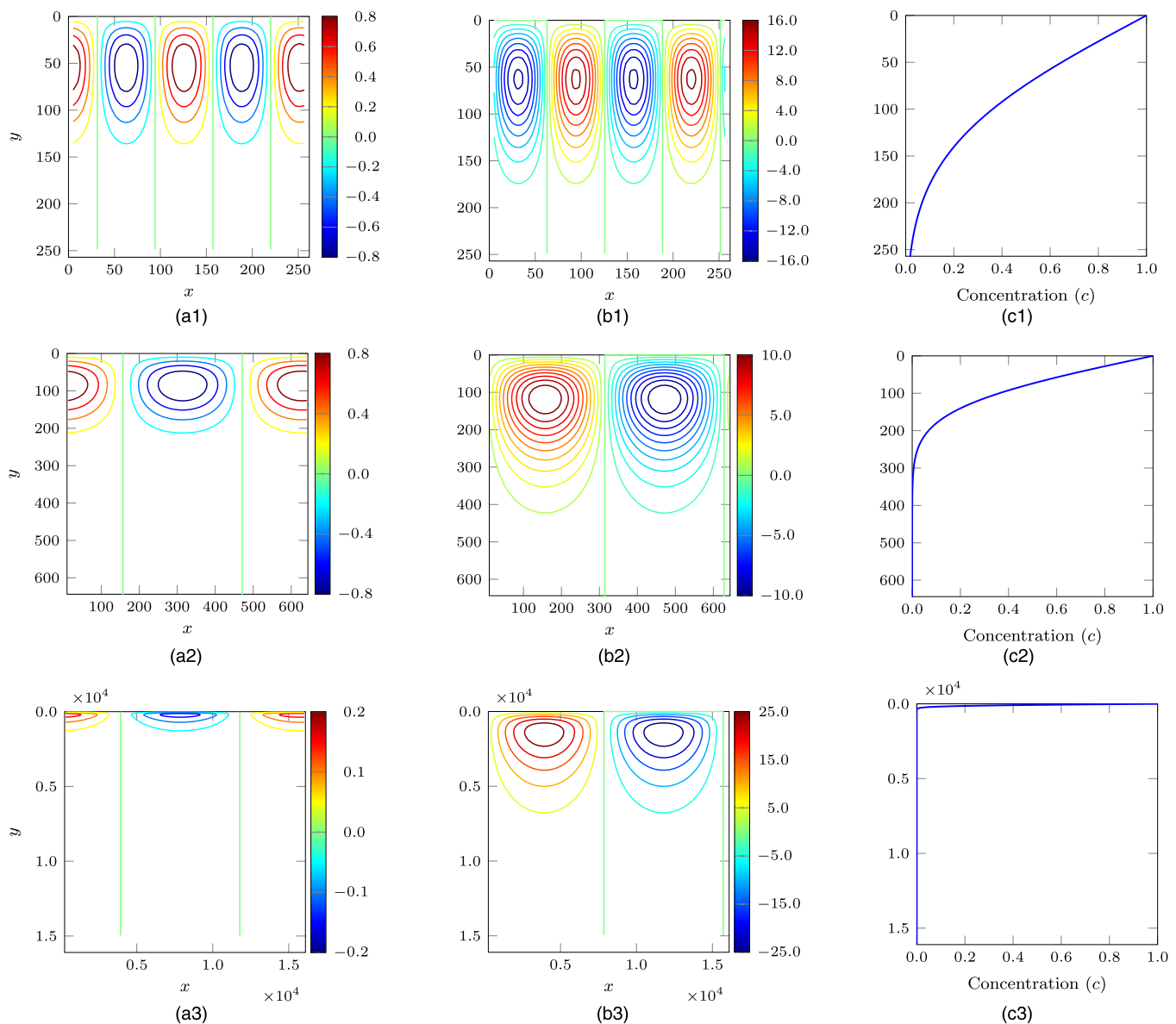


**FIG. 7.** Case of horizontal interface ( $\theta = 0$ ) at time  $t = 6.0 \times 10^3$  and wavenumber  $k = 5.0 \times 10^{-2}$  (row 1),  $k = 1.0 \times 10^{-2}$  (row 2), and  $k = 4.0 \times 10^{-2}$  (row 3): (a.) concentration; (b.) stream-function eigenmodes; and (c.) base state solution.

The analysis of the eigenmodes provides a physical reasoning as to why the growth curves are non-monotonic at times  $10^3 < t < 10^4$  (for example), namely, why are there intermediate wavenumbers which are stable, while larger and smaller wavenumbers are unstable. A key to the understanding of the suppression mechanism is given by the LSA equations themselves, which show that, as the layer is inclined, the convection effect due to the base state is increased, causing the eigenmodes to become tilted, and eventually increasing the diffusion effect, decreasing the growth rate of

the modes as the inclination is increased, eventually causing the dumping of all perturbation modes. One possible way of interpreting the non-monotonic results is that, for a given angle and a certain time, there are shallow modes, mostly associated to large wavenumbers, and deep modes, associated to small wavenumbers [see Fig. 5(a)]. Shallow modes are mostly immersed inside the concentration boundary layer of the base profile, as can be seen in Fig. 8 (first row), while deep modes reach largely outside of the boundary layer (see Fig. 8—fourth row). As the wavenumber is

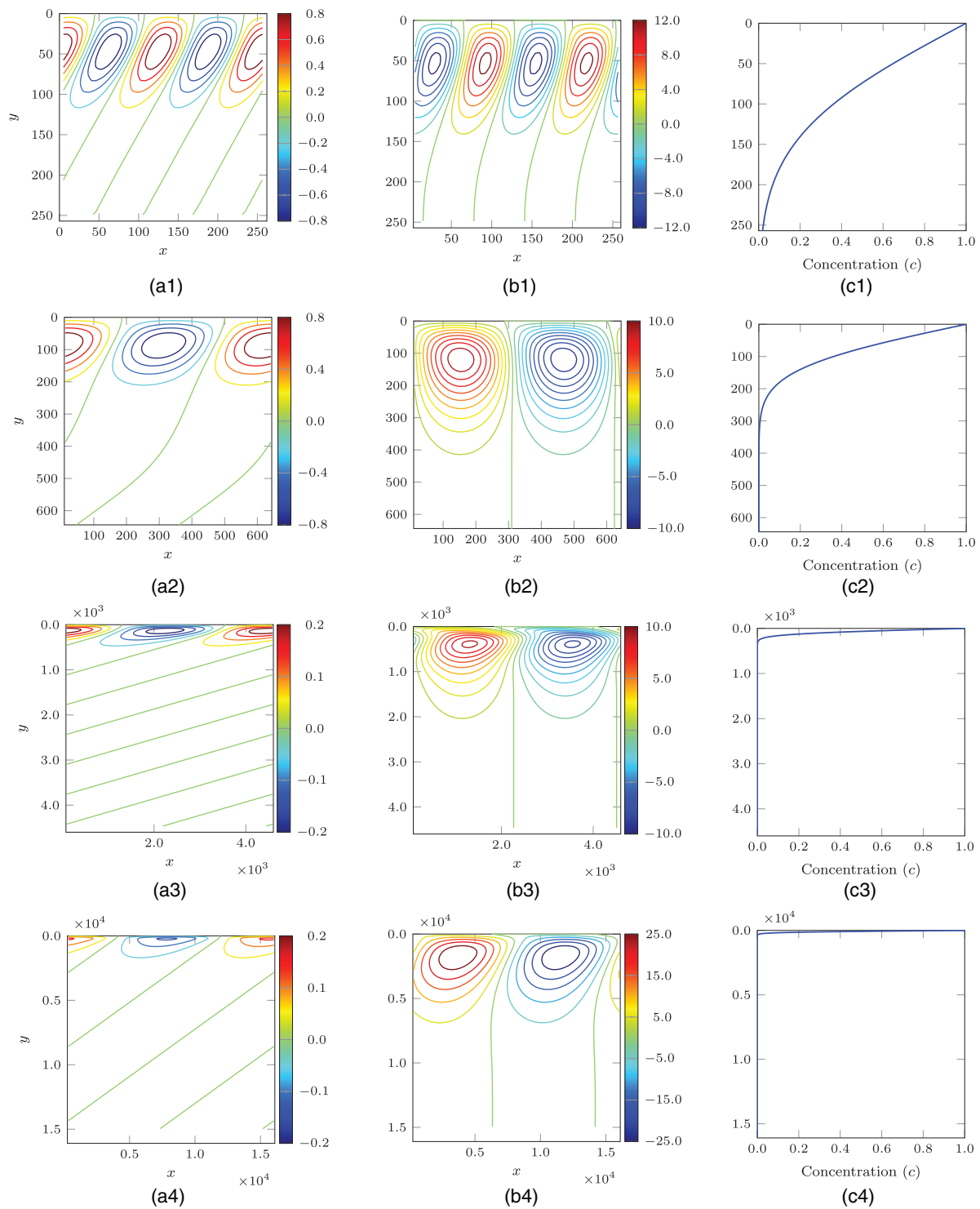


**FIG. 8.** Case of inclined interface ( $\theta = \pi/12$ ). Row 1:  $t = 6.0 \times 10^3$  and  $k = 5.0 \times 10^{-2}$ ; row 2:  $t = 6.0 \times 10^3$  and  $k = 1.0 \times 10^{-2}$ ; row 3:  $t = 4.8 \times 10^3$  and  $k = 1.4 \times 10^{-3}$ ; and row 4:  $t = 6.0 \times 10^3$  and  $k = 4.0 \times 10^{-4}$ . (a.) concentration; (b.) stream-function eigenmodes; and (c.) base state solution.

decreased, the modes gradually extend to regions outside of the boundary layer; thus, intermediate wavenumbers are associated to intermediate depths (Fig. 8—third row), suffer a stronger effective shearing effect from the base velocity profile and, therefore, are more affected by the combined convective–diffusive effects. This mechanism explains why, at a given time, for large wavenumbers, there exists a range of shallow modes that is unstable, and for small wavenumbers, there is a range of deep modes that are unstable, leaving an intermediate range of intermediate modes that are stable. The range of small wavenumbers deep unstable modes eventually disappears for longer times, which can be attributed to the extension of the combined convective–diffusive effect to deeper modes as the time advances. However, these low wavenumber modes have very small growth rates and they are not critically unstable, as seen in Fig. 5 and, therefore, not dynamically relevant.

### 3. Large inclination

In the case of a largely inclined interface, ( $\theta = \pi/6$ ), the real space representations of the eigenmodes ( $c', \psi'$ ) are distinctively sheared, due to the presence of a strong convection effect from the base state velocity, as seen on Fig. 9. For larger inclinations ( $\theta = \pi/5$ , for instance), the LSA predicts the absence of unstable modes, up to  $t \leq 1 \times 10^6$ .

### 4. Perturbation energy balance

Further understanding on the effect of the inclination on the stability of the perturbations may be obtained by analyzing the energy budget of the concentration perturbation eigenmodes energy  $|\tilde{c}|^2$ . In this section, we will employ  $*$  to denote the complex conjugate of a general complex number.

Taking Eq. (47), and multiplying by the complex conjugate of  $\tilde{c}$ , namely,  $\tilde{c}^*$ , we obtain

$$\sigma \tilde{c} \tilde{c}^* = [(D^2 - k^2) \tilde{c}] \tilde{c}^* - \bar{c}_y \tilde{\psi} \tilde{c}^* - ik \bar{u} \tilde{c} \tilde{c}^*, \quad (68)$$

where the left-hand side (LHS =  $\sigma \tilde{c} \tilde{c}^*$ ) term represents the balance, the first term on the right-hand side (RHS<sub>1</sub> =  $[(D^2 - k^2) \tilde{c}] \tilde{c}^*$ ) is

the diffusion term, the second (RHS<sub>2</sub> =  $\bar{c}_y \tilde{\psi} \tilde{c}^*$ ) term is the production of concentration perturbation by the effect of the perturbation stream function on the base state concentration profile, and the third (RHS<sub>3</sub> =  $ik \bar{u} \tilde{c} \tilde{c}^*$ ) term is due to the shear from the base velocity on the perturbation.

The real part is given by

$$\sigma_R \tilde{c} \tilde{c}^* = \text{real}([(D^2 - k^2) \tilde{c}] \tilde{c}^*) - \bar{c}_y (\tilde{\psi}_R \tilde{c}_R + \tilde{\psi}_I \tilde{c}_I), \quad (69)$$

and the imaginary part is given by

$$\sigma_I \tilde{c} \tilde{c}^* = \text{imag}([(D^2 - k^2) \tilde{c}] \tilde{c}^*) - \bar{c}_y (\tilde{\psi}_I \tilde{c}_R - \tilde{\psi}_R \tilde{c}_I) - k \bar{u} \tilde{c} \tilde{c}^*. \quad (70)$$

Here, we can recognize the real part of the eigenvalue  $\sigma_R$  as the growth rate, and the imaginary part  $\sigma_I$ , related to the phase velocity of the perturbation,  $-\sigma_I/k$ . Employing the polar form in the complex plane, we can write  $\tilde{c} = |\tilde{c}| \exp(i\varphi_c)$ ,  $\tilde{\psi} = |\tilde{\psi}| \exp(i\varphi_\psi)$ ; thus,

$$\bar{c}_y (\tilde{\psi}_R \tilde{c}_R + \tilde{\psi}_I \tilde{c}_I) = \bar{c}_y |\tilde{\psi}| |\tilde{c}| \cos(\varphi_\psi - \varphi_c). \quad (71)$$

Hence, the source of perturbation magnitude squared,  $|\tilde{c}|^2 = \tilde{c} \tilde{c}^*$ , depends critically on the relative phases  $\varphi_\psi - \varphi_c$ , being maximum when the two perturbations are on the same phase.

On the other hand, a glimpse on the effect of the inclination of the interface on the relative phases is provided by the analysis of the imaginary part, Eq. (70), where

$$\sigma_I \tilde{c} \tilde{c}^* = \text{imag}([(D^2 - k^2) \tilde{c}] \tilde{c}^*) - \bar{c}_y |\tilde{\psi}| |\tilde{c}| \sin(\varphi_\psi - \varphi_c) - k \bar{u} \sin \theta |\tilde{c}|^2. \quad (72)$$

From this expression, it can be observed that when  $\theta = 0$ , the relative phases difference  $\varphi_\psi - \varphi_c$  is null, and as the inclination angle  $\theta$  increases, the relative phase angle will also increase. In other words, as the inclination angle  $\theta$  increases, the concentration perturbation and the stream-function perturbation become less correlated, decreasing the growth rate of the eigenmode.

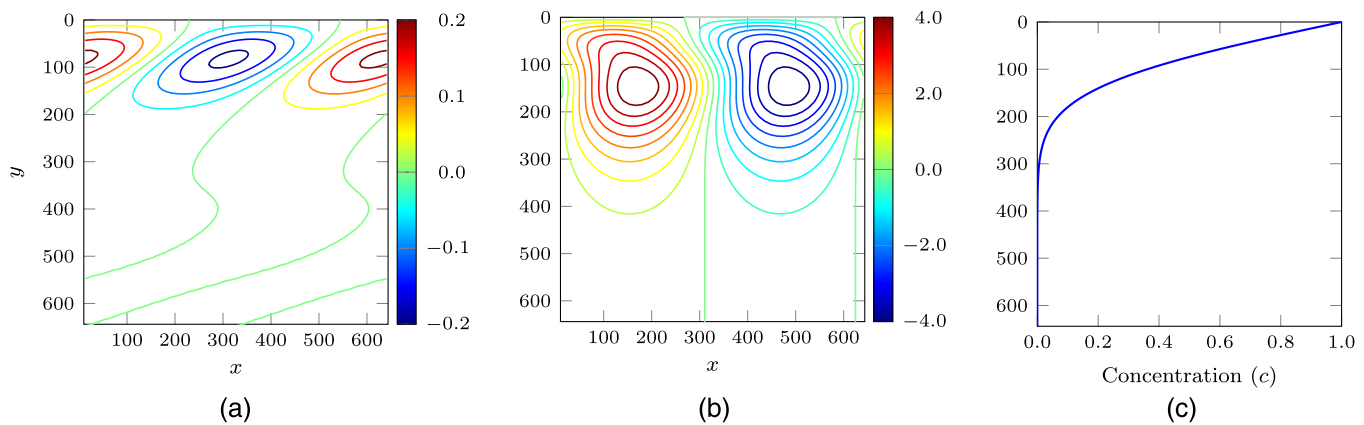


FIG. 9. Case of inclined interface ( $\theta = \pi/6$ ) at time  $t = 6.0 \times 10^3$  and wavenumber  $k = 1.0 \times 10^{-2}$ : (a) concentration; (b) stream-function eigenmodes; and (c) base state solution.

Another effect of the inclination can be observed on the perturbation vorticity  $\tilde{\omega}$ ,

$$\tilde{\omega} = -(D^2 - k^2)\tilde{\psi} = (k^2 \cos(\theta) + ik \sin \theta D)\tilde{c}. \quad (73)$$

Again, from this expression, we can observe that, when  $\theta = 0$ , vorticity, the stream function, and concentration perturbations are perfectly in phase (since all terms are pure real numbers), while as  $\theta$  increases the relative phases difference between the stream function and the concentration perturbations also increases, and, therefore, the in-phase contribution of the vorticity to the stream function decreases. In other words, as the inclination angle  $\theta$  increases, the concentration perturbation and the stream-function perturbation become less correlated, decreasing the growth rate of the eigenmode.

We may observe that, even though both mechanisms carry a similar trend with respect to the effect of the inclination angle  $\theta$ , the two are related to different terms of the equation: the first is the feedback mechanism that pumps energy onto the concentration perturbation from the gradient of the base concentration profile by means of the stream function, and the second is the source term of the stream function, which feeds directly from the concentration perturbation. Hence, the effect of the inclination angle of the interface  $\theta$  on the growth rate of the modes,  $\sigma_R$ , is twofold but, in appearance, the same.

The contributions of the diffusion, production, and shearing terms in the  $|\tilde{c}|^2$  budget, along with the relative angle  $\varphi_\psi - \varphi_c$ , for various inclinations are shown in Fig. 10. The real part budget shows that the (negative) diffusion term is not greatly influenced, while the

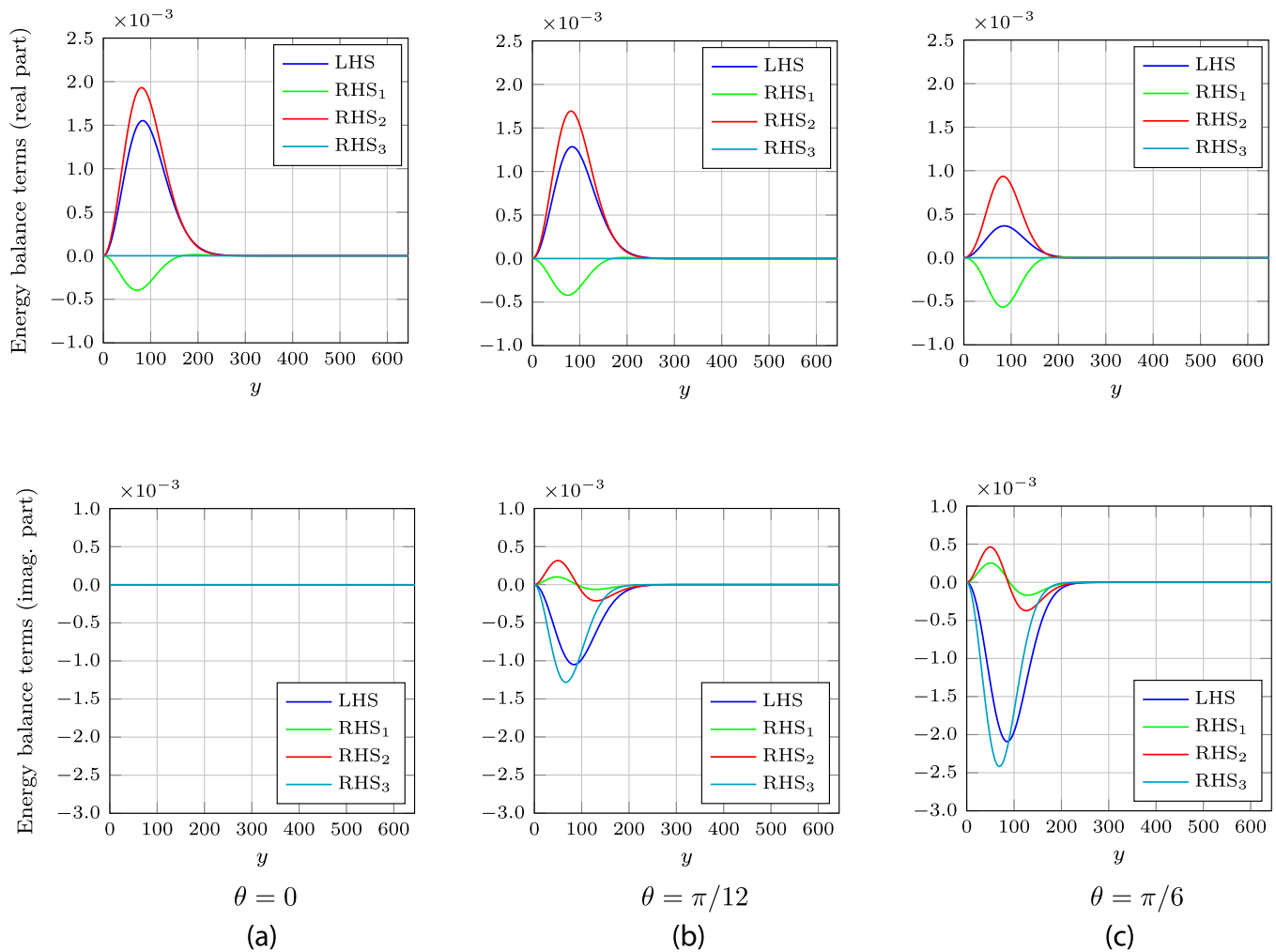


**FIG. 10.** Budget of the concentration perturbation eigenmodes energy  $|\tilde{c}|^2$ . The left-hand side (LHS =  $\sigma \tilde{c} \tilde{c}^*$ ) term represents the balance, the first term on the right-hand side (RHS<sub>1</sub> =  $[(D^2 - k^2) \tilde{c}] \tilde{c}^*$ ), is the diffusion term, the second (RHS<sub>2</sub> =  $\tilde{c}_y \tilde{\psi} \tilde{c}^*$ ) term is the production of concentration perturbation by the effect of the perturbation stream function on the base state concentration profile and the third (RHS<sub>3</sub> =  $ik \tilde{u} \tilde{c} \tilde{c}^*$ ) term is due to the shear from the base velocity on the perturbation. Cases (a)  $\theta = 0$ , (b)  $\theta = \pi/12$ , and (c)  $\theta = \pi/6$  with  $t = 6 \times 10^3$  and  $k = 1 \times 10^{-2}$ . (a)  $\theta = 0$ , (b)  $\theta = \pi/12$ , (c)  $\theta = \pi/6$ .

production term decreases, as the inclination angle  $\theta$  is increased, until eventually the budget becomes null or negative, for  $\theta > \pi/5$ . The imaginary part budget shows the increasing contribution of the production term to the imaginary part of the eigenvalue ( $\sigma_I$ ), as the relative angle  $\varphi_\psi - \varphi_c$  increases.

The behavior shown in this section is representative of perturbations with very small amplitude. In order to analyze the dynamics of finite amplitude perturbations, we perform a stability analysis through direct numerical simulations.

## V. NUMERICAL SIMULATIONS

### A. Formulation

The direct numerical simulation of the nonlinear perturbation evolution is obtained by the numerical solution of the nonlinear coupled Darcy's law [Eq. (12)], obtaining  $\psi$ , the stream function, and Eq. (13) for the concentration transport equation. We consider periodic boundary conditions at  $x = 0$  and at  $x = L_x$ , and impermeable walls at  $y = 0$  and at  $y = L_y$ , with  $c = 1$  on  $\Gamma_t$ , and  $\partial c/\partial y = 0$  on  $\Gamma_b$ . The initial conditions are given by  $\mathbf{u} = 0$  and  $c = 0$  in  $\Omega$  and  $c(x, y, t = 0) = 1 + 2(\xi - 1/2) \times 10^{-3}$  at the interface ( $\Gamma_t$ ), where  $\xi$  is a random number in the range  $[0, 1]$ .

### B. Numerical implementation with finite element method

The governing equations are solved using a finite element method,<sup>32,51</sup> where the differential equations and their boundary conditions are solved in weak form employing the Galerkin method with linear triangular elements.

The system of equations is solved in two steps. In the first one, we obtain the stream function. Velocity components are then obtained and introduced in the transport equation, which is subsequently solved. An LU factorization is applied as a preconditioner to the matrices and the linear systems and the velocity field from the stream-function solutions are then solved with the use of GMRES (Generalized Minimal Residual) solver. The computational implementation is performed in a C Programming Language in house code. LU factorization as well as GMRES routines from the PETSc library are utilized.<sup>52</sup> The computational parameters employed in the simulations are given in Table I.

The chosen value of  $\mathcal{R}a_y = 12\,000$  is sufficiently large to experience all the phases of convective dissolution (see Slim<sup>16</sup>). The value of  $\mathcal{R}a_x = 4000$  is sufficiently large to capture a significant number of fingers. The computational parameters ( $n_x$ ,  $n_y$ ,  $\Delta t$ , and  $\varepsilon$ ) were determined by a convergence study, showing grid independence.

### C. Characterization of the fingering structure

Here, we present the characterization procedure of the nonlinear dynamics of the concentration and velocity fields.<sup>16,37</sup>

Given the bidimensional concentration and velocity fields, we obtain the averaged profiles in each direction at successive times. The transverse average concentration profile is defined as

$$\langle c(y, t) \rangle = \frac{1}{L_x} \int_0^{L_x} c(x, y, t) dx, \quad (74)$$

TABLE I. Nondimensional parameters used in the simulations.

Parameter		Simulated value
$\mathcal{R}a_x = L_x$	Dimensionless width	4 000
$\mathcal{R}a_y = L_y$	Dimensionless length	12 000
$a_r$	Aspect ratio	1/3
$n_x$	Number of points along $x$ -direction	801
$n_y$	Number of points along $y$ -direction	2 401
$n_{el}$	Number of triangular elements	3 840 000
$\Delta x$	Horizontal uniform spacing	5.0
$\Delta y$	Average vertical spacing	5.0
$\Delta t$	Time step	2.5
$t_0$	Initial time	0.0
$t_{end}$	End time ( $\theta = \pi/32, \pi/16$ and $\pi/8$ )	$1.0 \times 10^5$
$t_{end}$	End time ( $\theta = 0, \pi/12, \pi/6$ and $\pi/5$ )	$1.7 \times 10^5$
$\varepsilon$	GMRes tolerance	$1.0 \times 10^{-5}$

$\langle c(y, t) \rangle$  gathers information about the total amount of dissolved solute stored in a layer located at a distance  $y$ . In the diffusive regime, it coincides with the analytical solution and in the convective regime, it indicates which position in the  $y$ -direction the fingers have reached at a given time.

Analogously,

$$\langle u(y, t) \rangle = \frac{1}{L_x} \int_0^{L_x} u(x, y, t) dx, \quad (75)$$

$$\langle v(y, t) \rangle = \frac{1}{L_x} \int_0^{L_x} v(x, y, t) dx. \quad (76)$$

From these definitions, substituting in Eq. (9) we observe that

$$\langle u(y, t) \rangle = \sin \theta \langle c(y, t) \rangle, \quad (77)$$

and that, using the continuity equation,

$$\langle v(y, t) \rangle = 0. \quad (78)$$

The longitudinal averaged profile defined as

$$\langle c(x, t) \rangle = \frac{1}{L_y} \int_0^{L_y} c(x, y, t) dy, \quad (79)$$

gathers information about the level of interaction between fingers.

The transverse profile allows us to define the mixing length  $\delta_L$  as the distance between the upper interface and the tip of the finger with larger length. It is evaluated from the transverse average profile and is given by the minimum  $y$  coordinate such that  $\langle c(y, t) \rangle \geq 0.01$ , as a function of time. Therefore, the tip of the fingers with larger length is estimated by the  $y$ -position where the average transverse profile is equal to 0.01. In the diffusive regime,  $\delta_{L, \text{diffusive}} = 2\sqrt{t} \operatorname{erf}^{-1}(0.99)$ , where  $t$  is time.

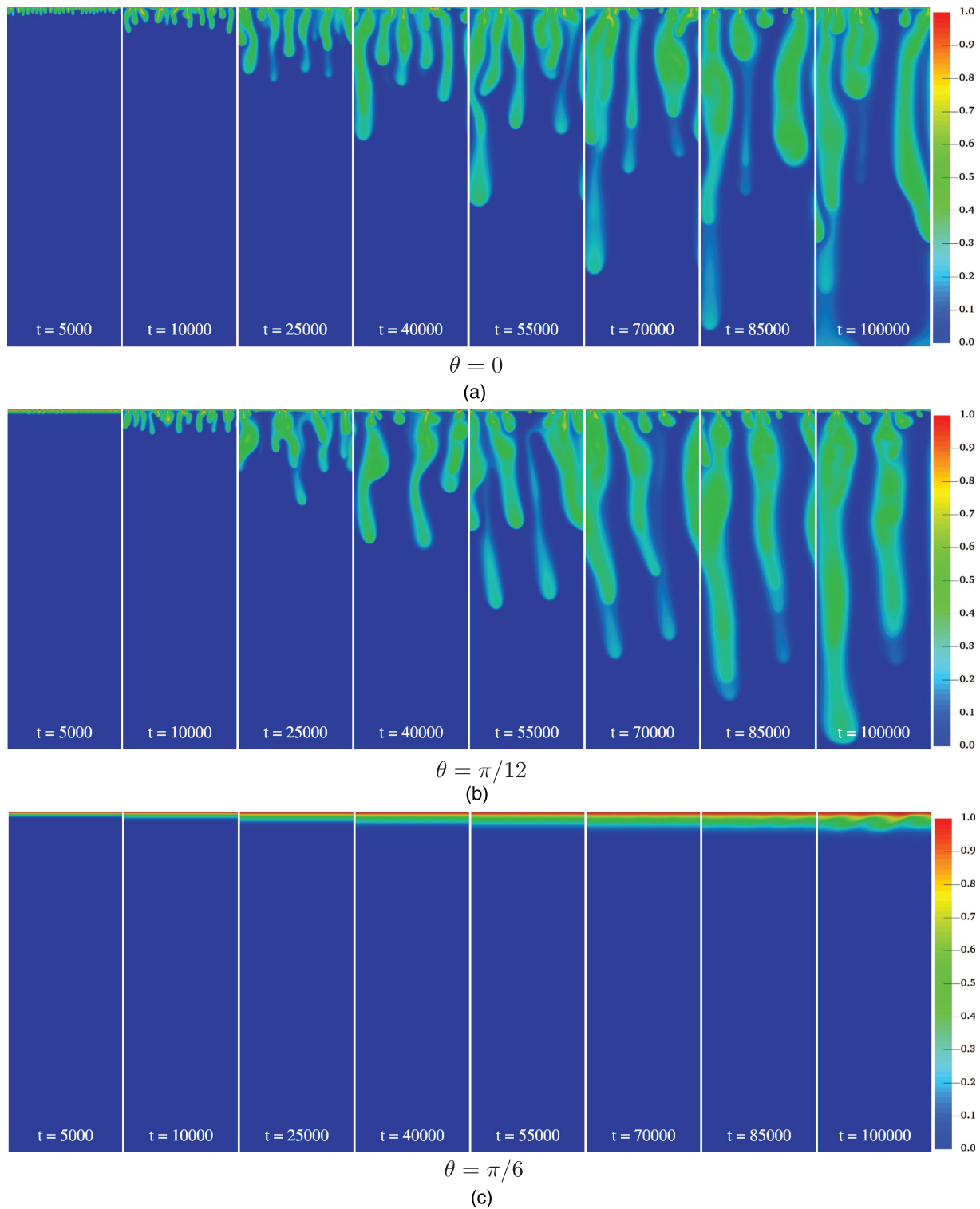


FIG. 11. Time evolution of the concentration field at times: 5000, 10 000, 25 000, 40 000, 55 000, 70 000, 85 000, and 100 000. (a)  $\theta = 0$ , (b)  $\theta = \pi/12$ , and (c)  $\theta = \pi/6$ .

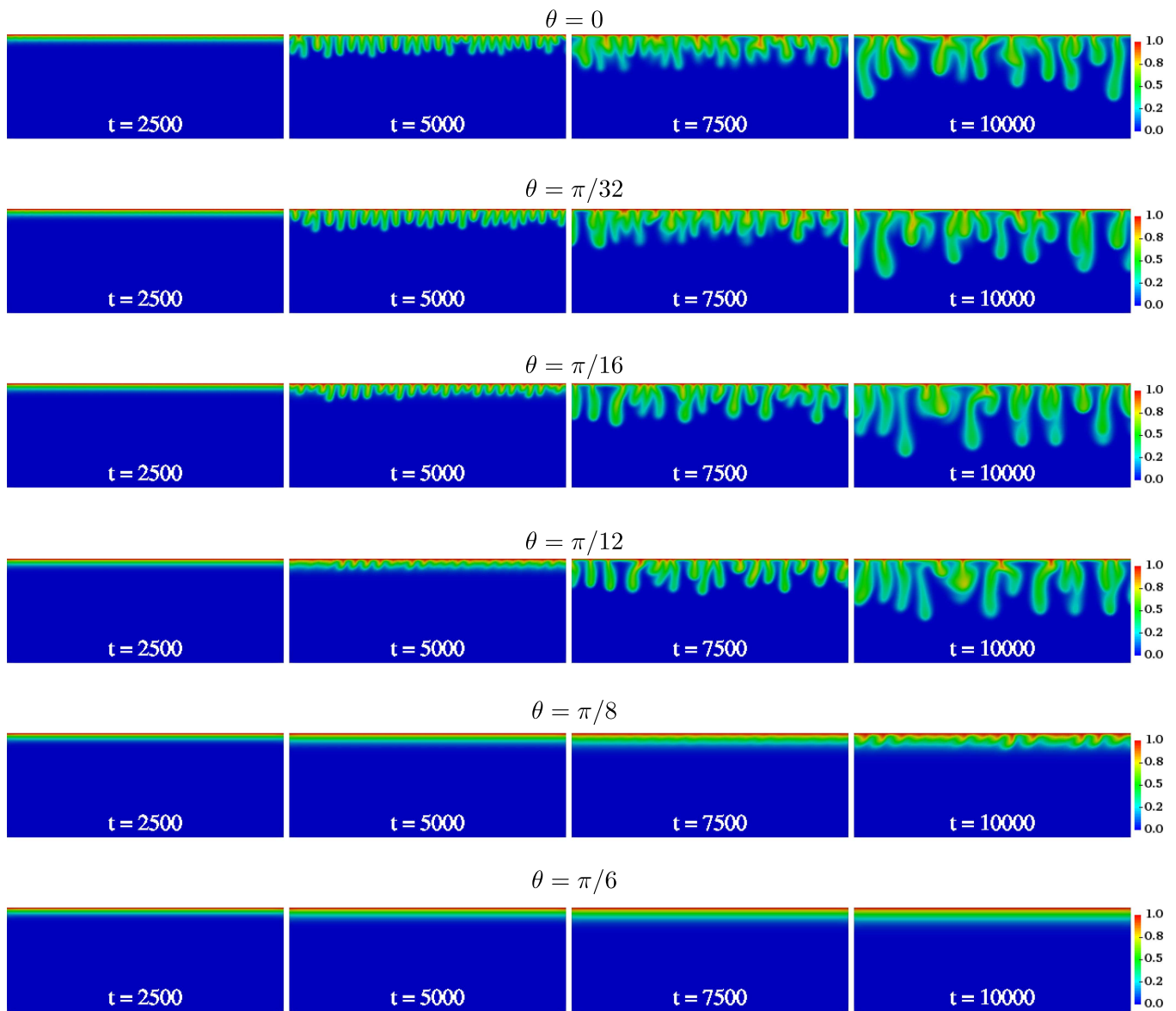


FIG. 12. Initial time evolution of the cases with  $\theta = 0, \theta = \pi/32, \theta = \pi/16, \theta = \pi/12, \theta = \pi/8$  and  $\theta = \pi/6$ , in times:  $t = 2500, 5000, 7500$ , and  $10\,000$ .

The area under the curve of the transverse profile,  $S$ , represents the amounts of solute dissolved in the host phase as a function of the time,

$$S = \int_0^{L_y} \langle c(y, t) \rangle dy. \tag{80}$$

In the case of the diffusive regime, the area is given by  $S_{\text{diffusive}} = 2\sqrt{t}/\sqrt{\pi}$ .

An important quantity is the dissolution flux  $F$ , defined as the rate at which the solute dissolves through the upper boundary.<sup>16,53</sup> It

is computed as

$$F = \frac{1}{L_x} \int_0^{L_x} \mathbf{n} \cdot \nabla c \Big|_{y=0} dl, \tag{81}$$

where  $dl = dx/n_y$ , and  $n_y$  is the  $y$  component of the unit normal vector. In the case of the diffusive regime, the dissolution flux is given by  $F_{\text{diffusive}} = 1/\sqrt{\pi t}$ . We remark that in the diffusive regime, there is no influence of the inclination angle  $\theta$  on the evolution of the concentration profile.

We also compute space-time maps of the concentration of the solute at a fixed distance  $\Delta y'$  from the upper boundary, saving the

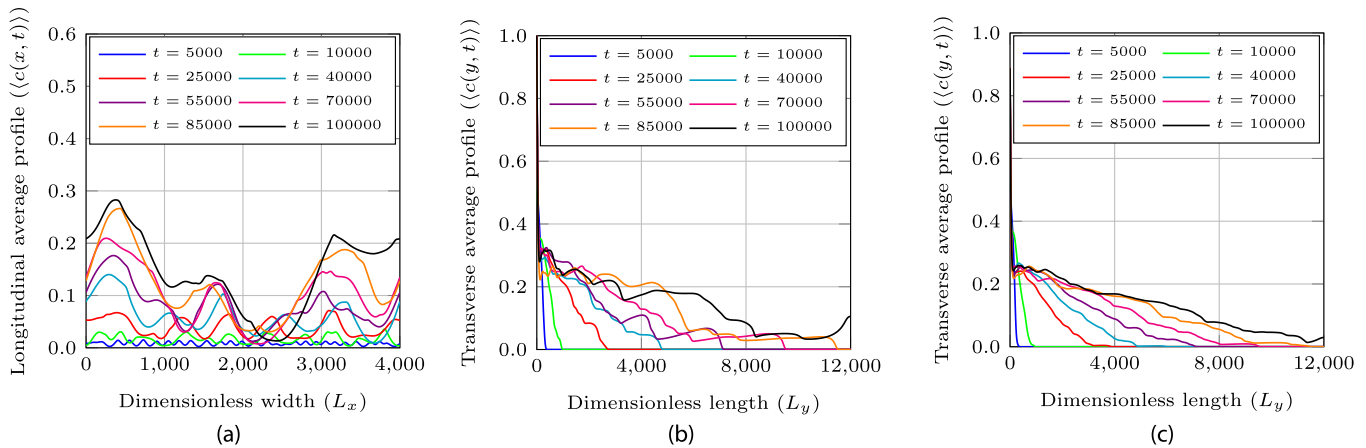


**FIG. 13.** (a) Longitudinal and (b) transverse averaged profiles for one realization; and (c) transverse averaged profiles obtained from an ensemble of nine realizations, of the case with  $\theta = 0$  in times: 5000, 10 000, 25 000, 40 000, 55 000, 70 000, 85 000, and 100 000.

concentration along the horizontal direction in time,  $c(x, \Delta y', t)$ . The distance  $\Delta y'$  was chosen sufficiently small to capture the onset of the fingers. The chosen value was 1% of the dimensionless height, which means  $\Delta y' = 120$ .

**D. Results**

Numerical simulations of the complete non-linear equations show the time evolution of the fingers for larger times. Figure 11 presents an overall picture of the dynamic evolution of the concentrations (blue is  $c = 0$ , red is  $c = 1$ ) when the inclination angle is varied. Fingers for cases with  $\theta > 0$  develop similarly to the case with  $\theta = 0$ ; however, they tend to drift toward the right, as predicted by the LSA. Additionally, a delay in the development of the fingers is visible from the concentration fields.

The time evolutions (Fig. 11) show an onset of fingers evenly distributed along the horizontal interface ( $\theta = 0$ ) at early times of evolution. However, a progressive coarsening to three to four main fingers is observed after  $t = 55 000$ .

The merging between fingers is enhanced in the inclined interface cases due to the drifting of the fingers caused by the inclination. This leads to an early stronger coalescence process in the case of larger inclinations, around time  $t = 25 000$  in case with  $\theta = \pi/12$  [see Fig. 11(b)].

However, for the inclination  $\theta = \pi/6$ , we can observe a delay in the beginning of the convective regime, where the diffusive regime lasts for a much longer time, practically up to around  $t = 100 000$ , when the convective regime finally begins to emerge [see Fig. 15(a), black curve for  $t = 100 000$ ]. In Sec. V D 6, this case is explored and discussed for later times.

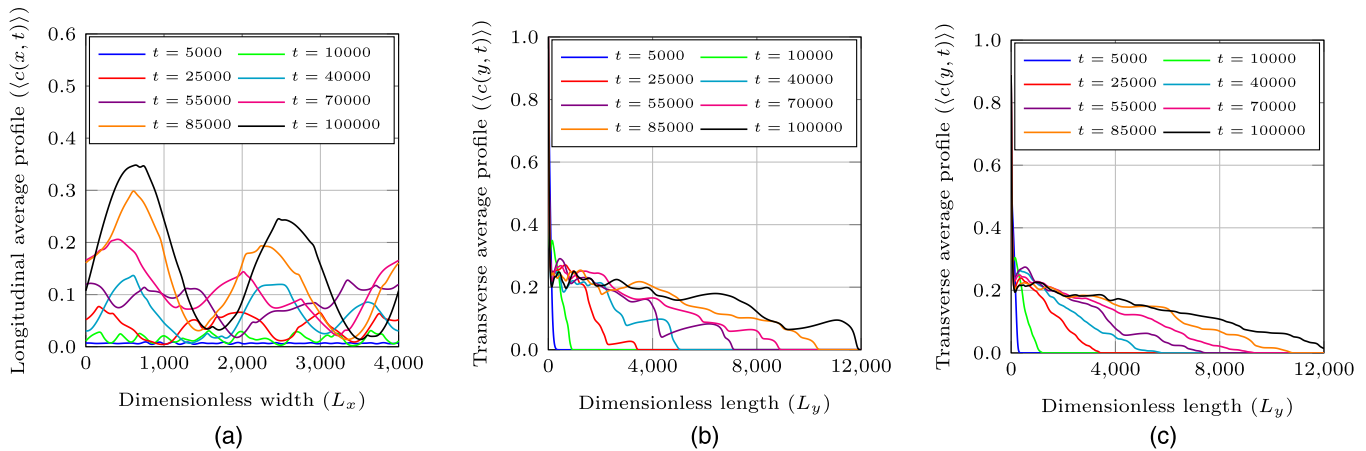


**FIG. 14.** (a) Longitudinal and (b) transverse averaged profiles for one realization; and (c) transverse averaged profiles obtained from an ensemble of nine realizations, of the case with  $\theta = \pi/12$  in times: 5000, 10 000, 25 000, 40 000, 55 000, 70 000, 85 000, and 100 000.

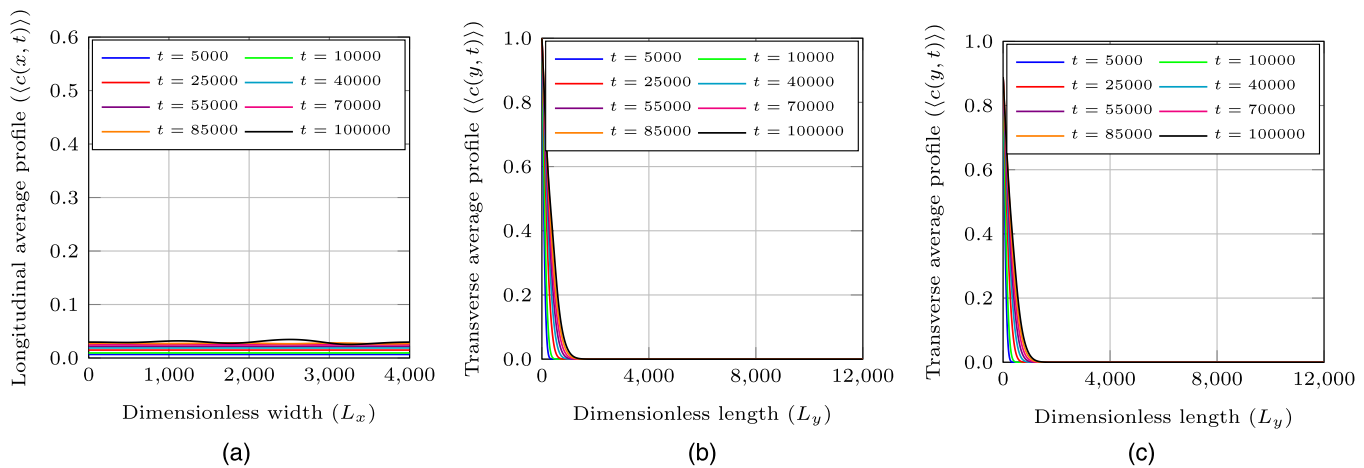


**FIG. 15.** (a) Longitudinal and (b) transverse averaged profiles for one realization; and (c) transverse averaged profiles obtained from an ensemble of nine realizations, of the case with  $\theta = \pi/6$  in times: 5000, 10 000, 25 000, 40 000, 55 000, 70 000, 85 000, and 100 000.

**1. Initial time evolution**

Figure 12 shows the initial time evolution of the cases with inclination angles:  $\theta = 0, \theta = \pi/32, \theta = \pi/16, \theta = \pi/12, \theta = \pi/8$  and  $\theta = \pi/6$ . The figure shows the beginning of the evolution in the diffusive regime and the transition to the convective regime that

occurs before time  $t = 5000$  for  $\theta = 0, \theta = \pi/32, \theta = \pi/16$ , and  $\theta = \pi/12$ , before  $t = 10\,000$  for  $\theta = \pi/8$ , while no transition occurs until  $t = 10\,000$  for the case  $\theta = \pi/6$ . Clearly, the interface inclination retards the convective process for angles of inclination greater than  $\theta = \pi/12$ .

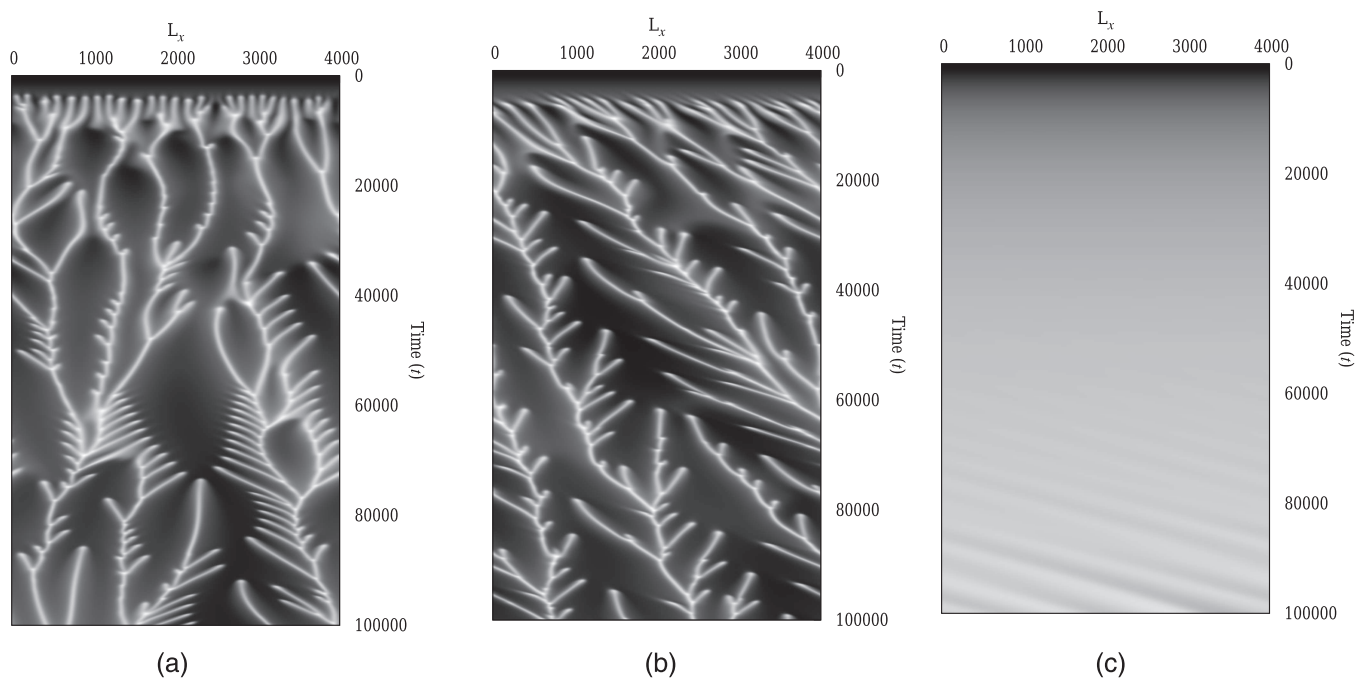


**FIG. 16.** Space-time maps of the cases: (a)  $\theta = 0$ ; (b)  $\theta = \pi/12$ ; and (c)  $\theta = \pi/6$ . The concentration of the solute along a line at  $y = 120$  is plotted along the horizontal axis of the figure, and time along the vertical one, increasing from  $t = 0$  at the top, to  $t_{\text{end}} = 100\,000$  at the bottom.

### 2. Transverse and longitudinal averaged profiles

Figures 13–15(a), at left, show the average longitudinal profiles,  $\langle c(x, t) \rangle$ , at successive times, associated to the results presented in Fig. 11 for inclined interfaces with  $\theta = 0, \pi/12$  and  $\pi/6$ , respectively. These profiles show the time evolution of the horizontal distribution of the concentration, where we can observe the onset, fusion, and collapse of fingers.

Figures 13–15(b), at right, show the corresponding average transverse profiles,  $\langle c(y, t) \rangle$  at successive times. The profiles give us a picture of the concentration distribution along the vertical direction. In the diffusive regime, we recover the analytical solution of this phase of the evolution. Once convection develops,  $\langle c(y, t) \rangle$  feature bumps due to the presence of fingers and the progression is faster thanks to convection. In Fig. 13(b), the transverse average profile shows that the fingers reach the bottom before the time  $t = 100\,000$ .

The transverse averaged profiles for a single simulation on the  $L_x = 4000$  domain are not sufficient to provide a completely converged statistical average. To produce more converged profiles, we have computed the transverse average profiles over an ensemble of nine realizations and plotted this smoother average, as shown in 13–15(c).

The results for  $\theta = \pi/12$  are representative of the effect of small inclination angles (see Fig. 14), that compared to a horizontal interface show a reduction of the undulations of the concentration profile at early times ( $t = 5000$ ), and better defined fingers at later times ( $t = 100\,000$ ). A different behavior for  $\theta = \pi/6$  can be observed, where the diffusive regime lasts for a much longer time, practically up to around  $t = 100\,000$ , when the convective regime finally begins to emerge, as can be seen in Figs. 11(c), 15, and 16(c).

### 3. Space-time maps

Figure 16 presents the space-time map associated to the simulations of the cases with  $\theta = 0, \theta = \pi/12$ , and  $\theta = \pi/6$ .

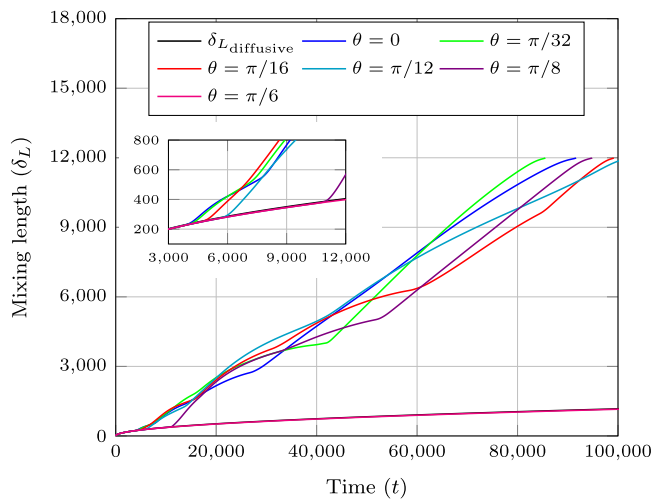


FIG. 17. Mixing length as a function of time of the cases with  $\theta = 0, \theta = \pi/32, \theta = \pi/16, \theta = \pi/12, \theta = \pi/8$ , and  $\theta = \pi/6$ .

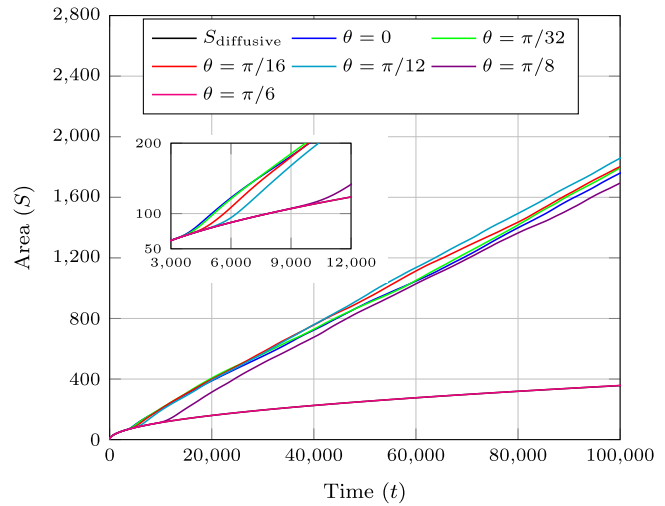


FIG. 18. Area of the averaged transverse profile as a function of time of the cases with  $\theta = 0, \theta = \pi/32, \theta = \pi/16, \theta = \pi/12, \theta = \pi/8$ , and  $\theta = \pi/6$ .

Concentration is plotted along the horizontal axis of the figure, and time, along the vertical one, increasing from  $t = t_0 = 0$  at the top, to  $t_{\text{end}} = 100\,000$  at the bottom. The figure shows the successive onset of fingers in the boundary layer and the merging of developed ones. The space-time maps (Fig. 16) show that, as  $\theta$  is increased, the drift velocity increases and the number of fingers decreases. For the case  $\theta = \pi/6$ , the instability starts to appear at around  $t = 70\,000$  but grows very slowly until  $t = 100\,000$ , without any fingering occurrence. Hence, the onset of the perturbations on the space-time maps appears at times roughly  $1.0 \times 10^1$  larger than the

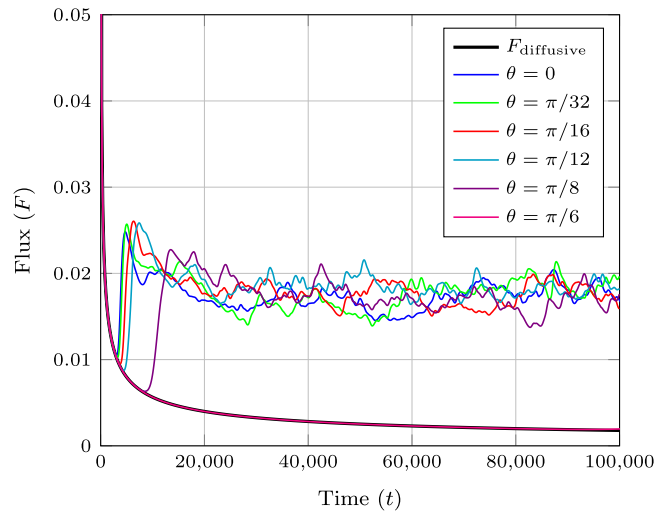


FIG. 19. Dissolution flux as a function of time of the cases with  $\theta = 0, \theta = \pi/32, \theta = \pi/16, \theta = \pi/12, \theta = \pi/8$ , and  $\theta = \pi/6$ .

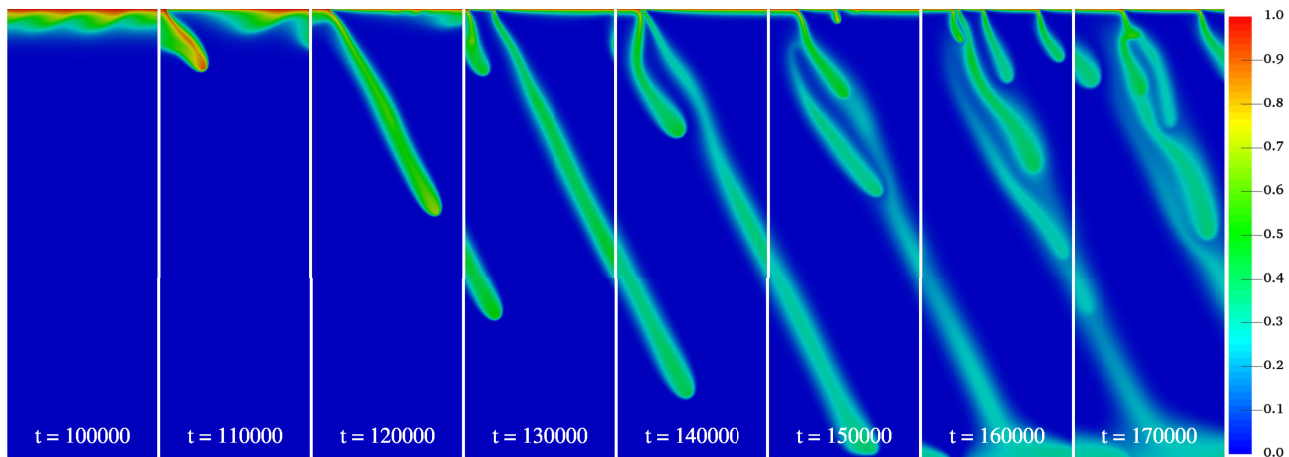


FIG. 20. Time evolution of the concentration field for the case with  $\theta = \pi/6$  from time  $t = 100\,000$  to  $t = 170\,000$ .

corresponding times for critical stability as predicted by the LSA (see Fig. 6). The associated wavenumber  $k \approx 4.7 \times 10^{-3}$  is within the range of unstable modes for  $t = 1.0 \times 10^5$ .

#### 4. Mixing length and area of the averaged transverse profile as a function of time

Figure 17 shows the temporal evolution of the mixing length for a horizontal and five inclined interfaces. This figure corroborates the fact that larger interface inclinations delay the beginning of the departure from the diffusive behavior. However, after an initial perturbation growth, all inclination cases undergo a large increase in the mixing length that compensates the initial delay, such that at around  $t = 15\,000$  all cases with  $0 < \theta < \pi/8$  have approximately the same mixing length. Note that, for  $\theta = \pi/6$ , stabilization induces the recovery of a diffusive growth of the mixing length for much longer times.

Figure 18 plots the time evolution of the total amount of solute, for a horizontal as well as inclined interfaces obtained, as described in Sec. V C. The plots show that systems with inclined interfaces with small angles,  $0 < \theta < \pi/12$ , dissolve almost the same amount of solute, up to  $t = 10\,000$ , while inclined interfaces with larger angles suffer a reduction on the area at these early times due to the delay on the convective regime. However, for larger times, inclined interfaces behave in a slightly different manner, increasing from  $\theta = 0$  to a maximum amount for the  $\theta = \pi/12$  angle, and then decreasing for larger angles.

We must remark that the above averaged quantities are computed taking  $L_x$  as reference, which is the length along the (inclined) interface. If we take as reference the horizontal length  $L_h = L_x / \cos\theta$ , the amount of solute will be *increased* by a factor  $1/\cos\theta$ . Hence, in cases with small angles, the inclination favors a larger amount of solute to be transferred to the porous medium.

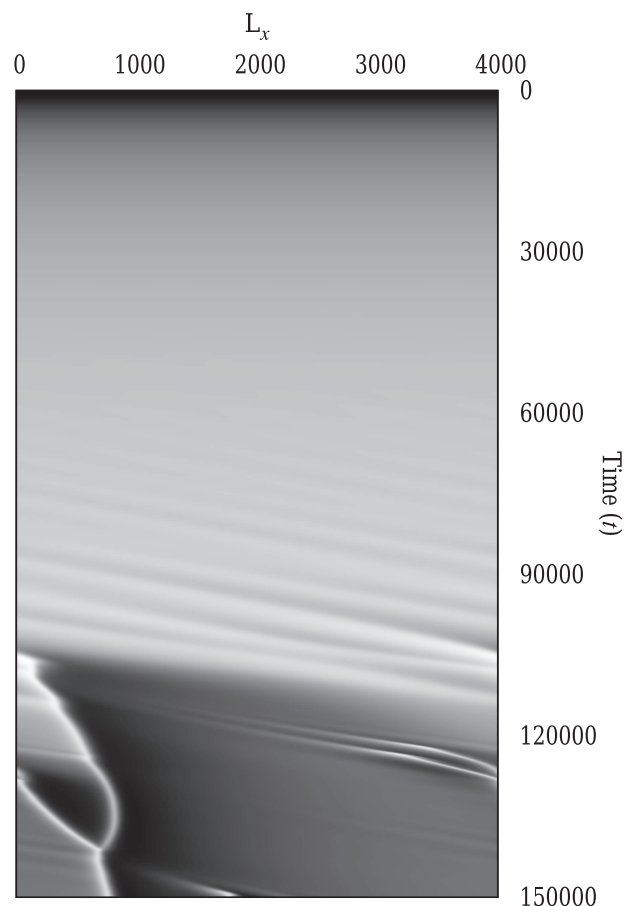


FIG. 21. Space-time map of the case with  $\theta = \pi/6$  at long times.

5. Dissolution flux through of the upper boundary

The dissolution flux,  $F$ , defined as the rate at which the solute dissolves through the upper boundary, provides an additional insight about the effect of the interface inclination on the amount of solute dissolved in the porous medium. Figure 19 shows the flux as a function of time for the considered horizontal and inclined interfaces. It can be observed that, for all angles, the wall flux has initially a diffusive behavior, closely following the theoretical curve  $F_{\text{diffusive}} = 1/\sqrt{\pi t}$ , until the emergence of the convective regime. This figure confirms the result given in Fig. 18, i.e., inclined interfaces lead to a delay in the onset of the convective regime. For small angles, the flux reaches, after a transition time, a convective regime plateau which is not very sensitive to small angle variations. For angles larger than  $\theta = \pi/6$ , the convective regime is completely suppressed for the range of analyzed times and the wall flux closely follows the characteristic diffusive decreasing trend of  $F_{\text{diffusive}}$  up to  $t = 1 \times 10^5$ . The  $\theta = \pi/6$  case will be further analyzed in Sec. VD 6.

6. Results of the case with  $\theta = \pi/6$ , for  $t \geq 100\,000$

In this subsection, we will address the long-time behavior for the case  $\theta = \pi/6$  and compare to horizontal ( $\theta = 0$ ) and small inclination ( $\theta = \pi/12$ ) cases. This will allow to stress that the convective regime develops much later for larger inclinations and will be eventually suppressed by angles  $\theta > \pi/5$ .

Figure 20 shows the evolution of fingering, at long times, from  $t = 100\,000$  up to  $t = 170\,000$ , for the case of largest slope considered,  $\theta = \pi/6$ . For this case, fingers develop only after a substantial growth of the concentration boundary layer and accumulation of the solute at the top of the domain. This result is consistent with previous findings that large interface inclinations cause inhibition of the growth of disturbances.<sup>32</sup>

The same qualitative suppression mechanism has been observed on “two-sided” systems in previous works.<sup>28,29</sup> In particular, Wen and Chini<sup>28</sup> also report a dramatic change on the dynamics of the “two-sided” system for angles  $\theta > 30$ , with the complete breakdown of the columnar flow and transition to a large-scale traveling-wave convective roll state, and significant reduction of the transport.

The space–time map for  $\theta = \pi/6$  (see Fig. 21) clearly depicts the very slow transition and delayed onset of the convective regime. In agreement with the LSA results, perturbations start to grow at much later times and grow very slowly until a first finger structure appears at approximately  $t = 100\,000$ , followed by a second one after a large time interval. This behavior is also consistent with the inhibition of the growth of perturbations observed in the case of large interface inclinations in the LSA. In fact, for  $\theta = \pi/6$ , fingers develop only at much later times.

Once individual fingers detach from the boundary layer, they descend at an angle of approximately  $\pi/6$  with respect to the surface normal when they do not interact with other fingers. Additionally, each descending finger drags the boundary fluid layer on its root, causing a depletion of solute, an efficient transport to the deeper layers, and a sharp increase in mixing length [see Fig. 22(a)], total solute amount [area in see Fig. 22(b)], and flux at the surface [see Fig. 23(a)]. The boundary fluid depletion occurs at much earlier times in cases with smaller or zero inclination angle. However, the boundary layer depletion is less obvious to visualize from the concentration fields (see Fig. 20), but since it is much more frequent and effective, it results in a pronounced increase in the flux. The long-time behavior of the dissolution flux through the upper boundary, Fig. 23(a), shows that the flux closely follows the diffusive flux  $F_{\text{diffusive}}$  up to the transition to the convective regime, that for  $\theta = \pi/6$  occurs at much later times (around  $t \approx 1 \times 10^5$ ).

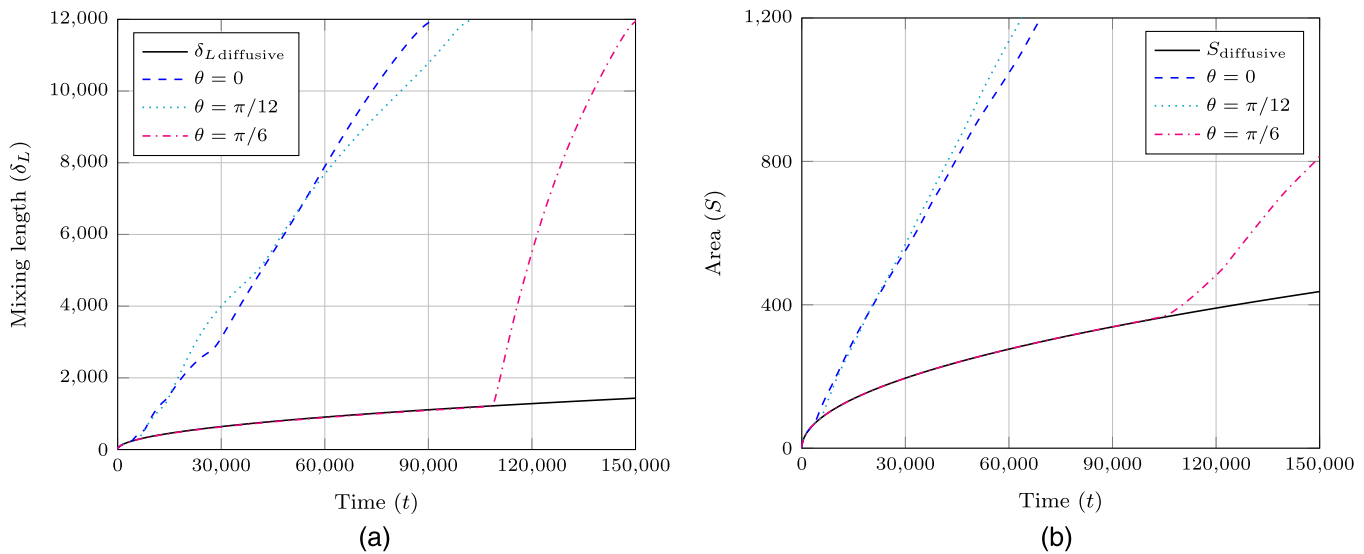
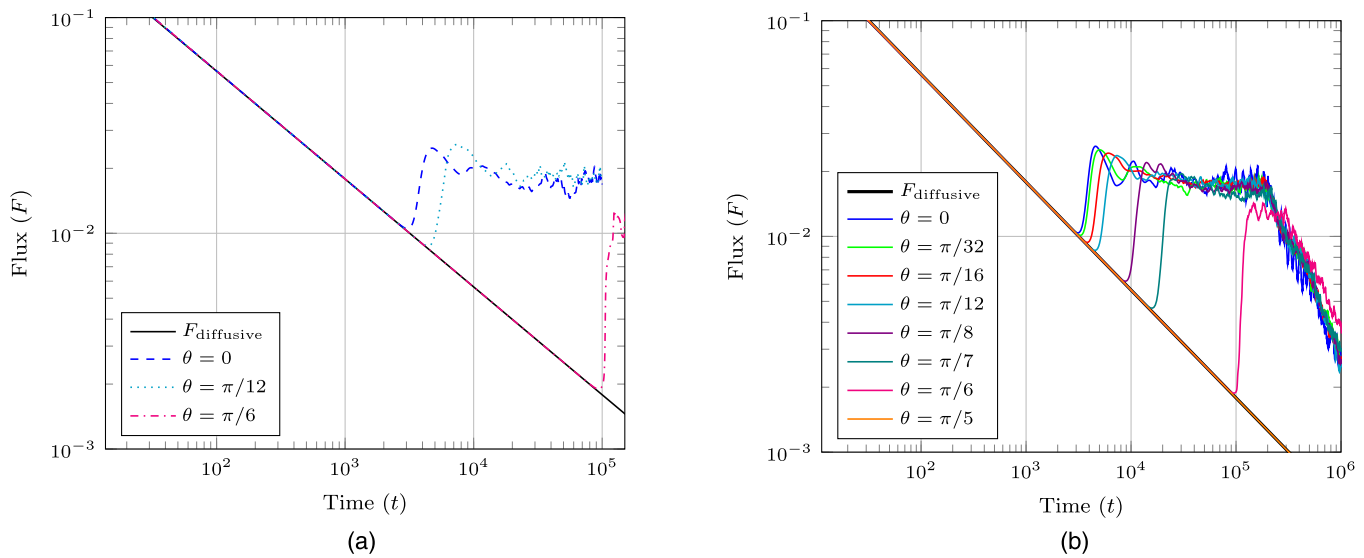


FIG. 22. (a) Mixing length and (b) area of the averaged transverse profile, both as a function of time for the case with  $\theta = \pi/6$  at long times, compared to the diffusive regime, the  $\theta = 0$ , and  $\theta = \pi/12$  cases.



**FIG. 23.** Dissolution flux through of the upper boundary: (a) for the case with  $\theta = \pi/6$  compared to the diffusive regime, the  $\theta = 0$ , and  $\theta = \pi/12$  cases, and (b) ensemble average of 9 realizations, for  $\theta = 0, \pi/32, \pi/16, \pi/12, \pi/8, \pi/7$ , and  $\pi/6$ . The flux for case  $\pi/5$  coincides with the diffusive solution,  $F_{\text{diffusive}}$ , up to  $t = 1 \times 10^6$ .

Additional simulations were performed to clarify the behavior of the dissolution flux in various regimes up to the shutdown of convection. Ensemble averages over nine realizations were employed to compute the time averaged dissolution rates and are shown in Fig. 23(b). The flux in the convective regime is approximately 0.017 as seen in Refs. 35 and 16, and references therein, for inclination angles  $\theta = 0, \pi/32, \dots, \pi/7$ , while for  $\theta = \pi/6$ , close to the critical value, it drops substantially and eventually, for  $\theta = \pi/5$ , reaches the values of diffusive regime, completely suppressing the convective plateau.

The transverse and longitudinal averaged profiles for  $\theta = \pi/6$  (see Fig. 24) show the late evolution of the concentration field after the inception of the convective regime. The transverse profiles are flattened partially by the fact that the fingers are strongly inclined. The transverse profiles [center, see Fig. 24(b)] show the progression of the finger tips until they reach the bottom of the domain. However, the transverse average profile shows that the fingers reach the bottom after the time  $t = 150\,000$ .

The delay in the onset time for the development of the fingers can be partially compensated by an increase in the magnitude

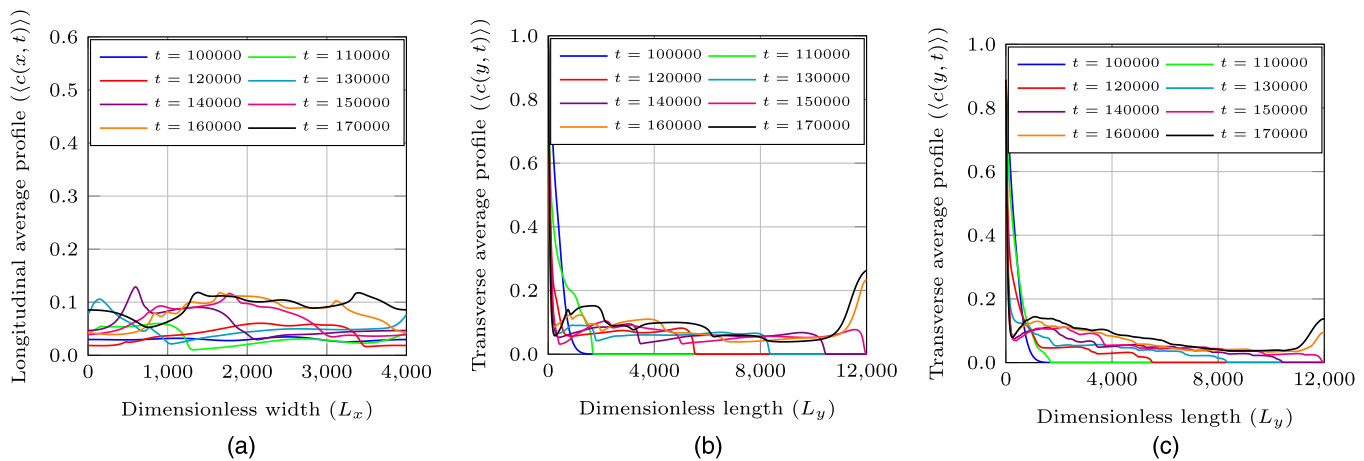


**FIG. 24.** (a) Longitudinal and (b) transverse averaged profiles for one realization; and (c) transverse averaged profiles obtained from an ensemble of nine realizations, of the case with  $\theta = \pi/6$  in times: 100 000, 110 000, 120 000, 130 000, 140 000, 150 000, 160 000, and 170 000.

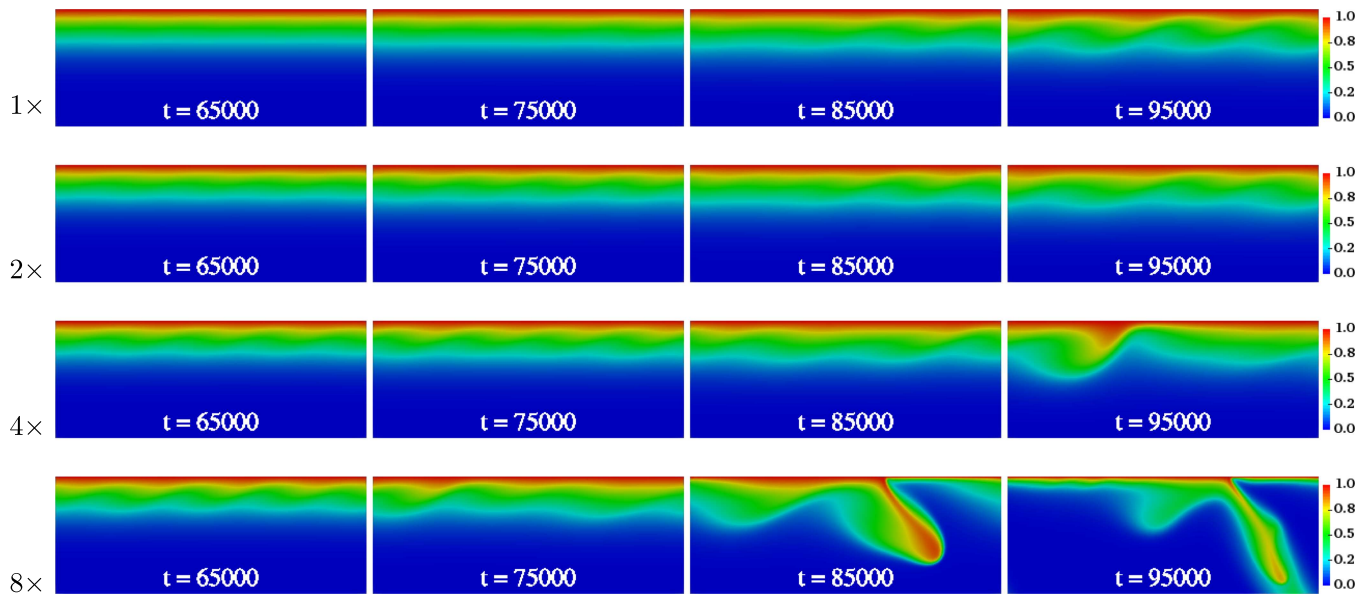


**FIG. 25.** Time evolution of the case with  $\theta = \pi/6$  with different amplitude of the seeding noise in the initial condition, in times:  $t = 65\,000$ ,  $75\,000$ ,  $85\,000$ , and  $95\,000$ . It can be observed that the perturbations are tilted backward while still in the boundary layer region, in a transitional convective regime, and then bend forward when in the fully convective fingering regime.

of the initial perturbation. Numerical experiments have shown that increasing the initial random perturbation by a factor of 8 can advance the time for the onset of the fingering instability from  $t = 95\,000$  to about  $t = 65\,000$ . Hence, the initial amplitude of the perturbations is not a very important factor on the onset time, as can be seen in Fig. 25. It can be observed that the perturbations are tilted backward while still in the boundary layer region, as the surface current transports the top layers with a larger  $x$ -velocity, and then bend forward when in the fully convective fingering regime, as they move deeper in the convective region, away from the top layer, where gravity is the main driving force.

### 7. Results of the case with larger inclination angles

For larger inclination angles, such as  $\theta = \pi/5$ , LSA and direct numerical simulations show that the diffusive regime is not disrupted by hydrodynamic instabilities; thus, no convective regime is observed.

These results, obtained for periodic (infinite) domains in the down-slope direction, contrast with cases where finite domains with impermeable lateral boundaries are used such as found in Ref. 15, where the accumulation of solute at the lower side of the interface leads to the formation of a strong downward wall current, and the appearance of a single large finger on the side of the wall, for any larger angle.

The dissolution rate, for larger inclination angles, which is the quantity of interest for predicting the dissolution time of carbon dioxide after injection, is found to be given by the diffusive dissolution rate,  $F_{\text{diffusive}}$ , for times up to  $t = 1.5 \times 10^5$ , in agreement with LSA results. A similar trend was also observed by Wen

and Chini,<sup>28,29</sup> for the problem of thermal convection in an inclined porous medium subject to a constant temperature difference. In a quite similar fashion, in their first study,<sup>28</sup> the Nusselt number,  $Nu$ , is only weakly dependent on  $\theta$  for  $\theta < 20^\circ$ , although there is a slight increase up to a maximum around  $\theta = 10^\circ$ . For  $\theta > 25^\circ$ , the columnar flow structure begins to break down and  $Nu$  decreases rapidly as  $\theta$  is increased further. In particular, for  $\theta \geq 32^\circ$ , the convection transitions to a large-scale traveling-wave convective flow. In the present problem, as the unsteady profile reaches the bottom of the domain, the concentration gradient is progressively reduced, thus inhibiting the appearance of large-scale perturbations at large times.

### VI. CONCLUSIONS

In this work, we considered the problem of buoyancy-driven fingering generated in an inclined porous host layer by the dissolution, from the top surface, of a partially miscible solute in a liquid host layer. The concentration of the solute in the fluid affects the density of the solution, thus producing buoyancy-driven flows. The interface between the dissolving layer and the host phase is inclined by an angle  $\theta$  relative to the horizontal direction.

We have analyzed using both LSA and nonlinear simulations the effect of varying the angle  $\theta$  on the properties of the convective dissolution dynamics. The LSA shows that the inclination of the interface decreases the growth rate of the instability, thereby reducing the range of unstable wavenumbers and increasing the onset time as the angle is increased. Moreover, an inclination introduces a drift velocity on the perturbations, which is observable in both the linear stability analysis and the nonlinear simulations. The effect of finite thickness of the inclined layer for large times is also

addressed, showing the complete inhibition of perturbation growth at long times, and the critical time after which no perturbations are unstable increases with the thickness of the layer,  $\mathcal{R}a_y$ , as also found in the case of horizontal layers.<sup>17</sup>

Results from the simulations using the full nonlinear equations confirm the trend presented by the LSA, showing a delay on the development of the convective instability as the angle is increased.

The mixing length evolution analysis corroborates that larger interface inclinations delay the beginning of the departure from the diffusive behavior. However, after an initial perturbation growth, cases with small inclination angles undergo a large increase in the mixing length that compensates for the initial delay, such that, at later times, all cases with  $0 < \theta < \pi/8$  have approximately the same mixing length.

Our results show that the total mass of the dissolved solute increases practically linearly in time in the convective regime with small variations in cases of small inclination angles. At earlier times, systems with inclined interfaces with small different angles,  $0 < \theta < \pi/12$ , present almost the same total solute mass, while inclined interfaces with larger angles suffer a reduction on the total mass of solute dissolved due to the delay on the convective regime. However, for larger times, inclined interfaces behave in a slightly different manner, the total dissolved mass increasing from  $\theta = 0$  to a maximum amount for the  $\theta = \pi/12$  angle, and then decreasing for larger angles.

We must remark that the averaged quantities are defined here taking the length  $L_x$  of the system along the (inclined) interface area as reference. If we take as reference the horizontal length  $L_h = L_x / \cos \theta$ , the amount of solute will be *increased* by a factor  $1 / \cos \theta$ . Hence, in cases with small angles, the inclination favors a larger amount of solute to be transferred to the porous medium.

Analysis of the dissolution flux confirms the result obtained by the total concentration mass curves, that inclined interfaces delay the onset of the convective regime. However, for small angles, after the delayed transition time, the flux reaches a plateau, which is not very sensitive to small angle variations. On the other hand, for angles larger than  $\theta = \pi/5$ , the convective regime is completely suppressed for the range of analyzed times.

Our results contribute to understanding the specificities of convective dissolution in unbound regions where the interface direction is arbitrary.

## ACKNOWLEDGMENTS

The authors acknowledge FAPERJ (Research Support Foundation of the State of Rio de Janeiro), CNPq (National Council for Scientific and Technological): 207341/2014-1/SWE, and CAPES (Coordination for the Improvement of Higher Education Personnel) for their financial support. A.D.W. acknowledges financial support from FRS-FNRS for the PDR “Control” project.

## AUTHOR DECLARATIONS

### Conflict of Interest

The authors have no conflicts to disclose.

## Author Contributions

**R. M. Lucena:** Conceptualization (equal); Methodology (equal); Validation (equal); Writing – original draft (equal); Writing – review & editing (equal). **J. Pontes:** Conceptualization (equal); Methodology (equal); Validation (equal); Writing – original draft (equal); Writing – review & editing (equal). **A. De Wit:** Conceptualization (equal); Methodology (equal); Validation (equal); Writing – original draft (equal); Writing – review & editing (equal). **G. R. Anjos:** Conceptualization (equal); Methodology (equal); Validation (equal); Writing – original draft (equal); Writing – review & editing (equal). **N. Mangiacacchi:** Conceptualization (equal); Methodology (equal); Validation (equal); Writing – original draft (equal); Writing – review & editing (equal).

## DATA AVAILABILITY

The data that support the findings of this study are available from the corresponding author upon reasonable request.

## REFERENCES

- <sup>1</sup>IPCC (Intergovernmental Panel on Climate Change), 2005, “Special report on carbon dioxide capture and storage,” Technical report, Prepared by Working Group III of the Intergovernmental Panel on Climate Change, United Kingdom and New York, NY, USA, 2005.
- <sup>2</sup>H. E. Huppert and J. A. Neufeld, “The fluid mechanics of carbon dioxide sequestration,” *Annu. Rev. Fluid Mech.* **46**, 255–272 (2014).
- <sup>3</sup>P. Cheng, M. Bestehorn, and A. Firoozabadi, “Effect of permeability anisotropy on buoyancy-driven flow for CO<sub>2</sub> sequestration in saline aquifers,” *Water Resour. Res.* **48**(9), W09539, <https://doi.org/10.1029/2011WR011799> (2012).
- <sup>4</sup>J. Ennis-King and L. Paterson, “Role of convective mixing in the long-term storage of carbon dioxide in deep saline formations,” *Soc. Petrol. Eng.* **10**(3), 8 (2003).
- <sup>5</sup>J. Ennis-King and L. Paterson, “Coupling of geochemical reactions and convective mixing in the long-term geological storage of carbon dioxide,” *Int. J. Greenhouse Gas Control* **1**(1), 86–93 (2007).
- <sup>6</sup>J. Ennis-King, I. Preston, and L. Paterson, “Onset of convection in anisotropic porous media subject to a rapid change in boundary conditions,” *Phys. Fluids* **17**, 084107 (2005).
- <sup>7</sup>K. Ghesmat and H. Hassanzadeh, “The impact of geochemistry on convective mixing in a gravitationally unstable diffusive boundary layer in porous media: CO<sub>2</sub> storage in saline aquifers,” *J. Fluid Mech.* **673**, 480–512 (2011).
- <sup>8</sup>I. Gunn and A. W. Woods, “On the flow of buoyant fluid injected into a confined, inclined aquifer,” *J. Fluid Mech.* **672**, 109–129 (2011).
- <sup>9</sup>I. Gunn and A. W. Woods, “On the flow of buoyant fluid injected into an aquifer with a background flow,” *J. Fluid Mech.* **706**, 274–294 (2012).
- <sup>10</sup>M. A. Hesse, F. M. Orr, Jr., and H. A. Tchelepi, “Gravity currents with residual trapping,” *J. Fluid Mech.* **611**, 35–60 (2008).
- <sup>11</sup>V. Loodts, L. Rongy, and A. De Wit, “Impact of pressure, salt concentration, and temperature on the convective dissolution of carbon dioxide in aqueous solutions,” *Chaos* **24**, 043120 (2014).
- <sup>12</sup>C. W. MacMinn and R. Juanes, “Buoyant currents arrested by convective dissolution,” *Geophys. Res. Lett.* **40**, 2017–2022, <https://doi.org/10.1002/grl.50473> (2013).
- <sup>13</sup>C. W. MacMinn, M. L. Szulczewski, and R. Juanes, “CO<sub>2</sub> migration in saline aquifers. Part 1. Capillary trapping under slope and groundwater flow,” *J. Fluid Mech.* **662**, 329–351 (2010).
- <sup>14</sup>C. W. MacMinn, M. L. Szulczewski, and R. Juanes, “CO<sub>2</sub> migration in saline aquifers. Part 2. Capillary and solubility trapping,” *J. Fluid Mech.* **688**, 321–351 (2011).
- <sup>15</sup>Q. Meng and X. Jiang, “Numerical analyses of the solubility trapping of CO<sub>2</sub> storage in geological formations,” *Appl. Energy* **130**, 581–591 (2014).

- <sup>16</sup>A. C. Slim, "Solulal-convective regimes in a two-dimensional porous medium," *J. Fluid Mech.* **741**, 461–491 (2014).
- <sup>17</sup>A. C. Slim and T. S. Ramakrishnan, "Onset and cessation of time-dependent, dissolution-driven convection in porous media," *Phys. Fluids* **22**(12), 124103 (2010).
- <sup>18</sup>C. Thomas, S. Dehaeck, and A. De Wit, "Convective dissolution of CO<sub>2</sub> in water and salt solutions," *Int. J. Greenhouse Gas Control* **72**, 105–116 (2018).
- <sup>19</sup>X. Xu, S. Chen, and D. Zhang, "Convective stability analysis of the long-term storage of carbon dioxide in deep saline aquifers," *Adv. Water Resour.* **29**, 397–407 (2006).
- <sup>20</sup>Y. Zhang, G. Yang, and S.-Q. Li, "Significance of conceptual model uncertainty in simulating carbon sequestration in a deep inclined saline aquifer," *J. Hazard. Toxic Radioact. Waste* **19**(3), 04014036 (2015).
- <sup>21</sup>A. Riaz, M. Hesse, H. A. Tchelepi, and F. M. Orr, Jr., "Onset of convection in a gravitationally unstable diffusive boundary layer in porous media," *J. Fluid Mech.* **548**, 87–111 (2006).
- <sup>22</sup>G. S. H. Pau, J. B. Bell, K. Pruess, A. S. Almgren, M. J. Lijewski, and K. Zhang, "High-resolution simulation and characterization of density-driven flow in CO<sub>2</sub> storage in saline aquifers," *Adv. Water Resour.* **33**, 443–455 (2010).
- <sup>23</sup>C. Cohen, M. Berhanu, J. Derr, and S. Courrech du Pont, "Buoyancy-driven dissolution of inclined blocks: Erosion rate and pattern formation," *Phys. Rev. Fluids* **5**, 053802 (2020).
- <sup>24</sup>H. E. Huppert and A. W. Woods, "Gravity-driven flows in porous layers," *J. Fluid Mech.* **292**, 55–69 (1995).
- <sup>25</sup>D. Vella and H. E. Huppert, "Gravity currents in a porous medium at an inclined plane," *J. Fluid Mech.* **555**, 353–362 (2006).
- <sup>26</sup>F. J. Guerrero, R. M. Prol-Ledesma, and N. Karimi, "Transient thermo-solutal convection in a tilted porous enclosure heated from below and salted from above," *Int. Commun. Heat Mass Transfer* **118**, 104875 (2020).
- <sup>27</sup>P. A. Tsai, K. Riesing, and H. A. Stone, "Density-driven convection enhanced by an inclined boundary: Implications for geological CO<sub>2</sub> storage," *Phys. Rev. E* **87**, 011003 (2013).
- <sup>28</sup>B. Wen and G. P. Chini, "Inclined porous medium convection at large Rayleigh number," *J. Fluid Mech.* **837**, 670–702 (2018).
- <sup>29</sup>B. Wen and G. P. Chini, "On moderate-Rayleigh-number convection in an inclined porous layer," *Fluids* **4**(2), 101 (2019).
- <sup>30</sup>D. R. Hewitt, "Vigorous convection in porous media," *Proc. R. Soc. A* **476**(2239), 20200111 (2020).
- <sup>31</sup>H. Emami-Meybodi, H. Hassanzadeh, and J. Ennis-King, "CO<sub>2</sub> dissolution in the presence of background flow of deep saline aquifers," *Water Resour. Res.* **51**(4), 2595–2615 (2015).
- <sup>32</sup>R. M. Lucena, "Numerical study of CO<sub>2</sub> dissolution in saline aquifers with deformed interface," Ph.D. thesis (Rio de Janeiro State University, 2016).
- <sup>33</sup>M. A. Budroni, L. A. Riolfo, L. Lemaigre, F. Rossi, M. Rustici, and A. De Wit, "Chemical control of hydrodynamics instabilities in partially miscible two-layer systems," *J. Phys. Chem. Lett.* **5**, 875–881 (2014).
- <sup>34</sup>C. Almarcha, P. M. J. Trevelyan, P. Grosfils, and A. De Wit, "Chemically driven hydrodynamic instabilities," *Phys. Rev. Lett.* **104**(4), 044501 (2010).
- <sup>35</sup>M. De Paoli, F. Zonta, and A. Soldati, "Dissolution in anisotropic porous media: Modelling convection regimes from onset to shutdown," *Phys. Fluids* **29**(2), 026601 (2017).
- <sup>36</sup>M. De Paoli, F. Zonta, and A. Soldati, "Rayleigh-Taylor convective dissolution in confined porous media," *Phys. Rev. Fluids* **4**, 023502 (2019).
- <sup>37</sup>A. De Wit, "Miscible density fingering of chemical fronts in porous media: Nonlinear simulations," *Phys. Fluids* **16**(1), 163–175 (2004).
- <sup>38</sup>J. S. Nijjer, D. R. Hewitt, and J. A. Neufeld, "The dynamics of miscible viscous fingering from onset to shutdown," *J. Fluid Mech.* **837**, 520–545 (2018).
- <sup>39</sup>C. Canuto, M. Y. Hussaini, A. Quarteroni, and T. A. Zang, *Spectral Methods in Fluid Dynamics* (Springer-Verlag, Berlin, 1988).
- <sup>40</sup>J. E. Weber, "Thermal convection in a tilted porous layer," *Int. J. Heat Mass Transfer* **18**(3), 474–475 (1975).
- <sup>41</sup>M. Sen, P. Vasseur, and L. Robillard, "Parallel flow convection in a tilted two-dimensional porous layer heated from all sides," *Phys. Fluids* **31**(12), 3480–3487 (1988).
- <sup>42</sup>S. L. Moya, E. Ramos, and M. Sen, "Numerical study of natural convection in a tilted rectangular porous material," *Int. J. Heat Mass Transfer* **30**(4), 741–756 (1987).
- <sup>43</sup>O. D. Makinde, "On the Chebyshev collocation spectral approach to stability of fluid flow in a porous medium," *Int. J. Numer. Methods Fluids* **59**(7), 791–799 (2009).
- <sup>44</sup>B. M. Shankar, J. Kumar, and I. S. Shivakumara, "Stability of natural convection in a vertical layer of Brinkman porous medium," *Acta Mech.* **228**(1), 1–19 (2016).
- <sup>45</sup>L. N. Trefethen, *Spectral Methods in Matlab* (SIAM, New York, 2000).
- <sup>46</sup>J. P. Boyd, "The optimization of convergence for Chebyshev polynomial methods in an unbounded domain," *J. Comput. Phys.* **45**, 43–79 (1982).
- <sup>47</sup>C. E. Grosch and S. A. Orszag, "Numerical solution of problems in unbounded regions: Coordinate transforms," *J. Comput. Phys.* **25**, 273–295 (1977).
- <sup>48</sup>M. Maleki, I. Hashim, and S. Abbasbandy, "Analysis of IVPS and BVPS on semi-infinite domains via collocation methods," *J. Appl. Math.* **2012**, 696574.
- <sup>49</sup>R. Baltensperger, "Improving the accuracy of the matrix differentiation method for arbitrary collocation points," *Appl. Numer. Math.* **33**(1–4), 143–149 (2000).
- <sup>50</sup>P. M. J. Trevelyan, C. Almarcha, and A. De Wit, "Buoyancy-driven instabilities of miscible two-layer stratifications in porous media and Hele-Shaw cells," *J. Fluid Mech.* **670**, 38–65 (2011).
- <sup>51</sup>T. J. R. Hughes, *The Finite Element Method: Linear Static and Dynamic Finite Element Analysis*, 1st ed. (Prentice-Hall, New Jersey, 1987).
- <sup>52</sup>Office of Advanced Scientific Computing Research, *PETSc Users Manual*, revision 3.7 edition, April 2016.
- <sup>53</sup>D. R. Hewitt, J. A. Neufeld, and J. R. Lister, "Convective shutdown in a porous medium at high Rayleigh number," *J. Fluid Mech.* **719**, 551–586 (2013).